Norwegian University
of Life Sciences

Master's Thesis 2021 30 ECTS
Faculty of Science and Technology

Screening of thermoelectric performance of half-Heusler materials and their alloys from first principles

Øven Andreas Grimenes
Master of Science in Technology
Environmental Physics and Renewable energy

This page is intentionally left blank.

Preface

The completion of this master's thesis marks the end of my five years as a student in Environmental Physics and Renewable Energy at the Norwegian University of Life Sciences (NMBU). During these years I have learned a lot and greatly enjoyed the time spent here, and for that, I would like to thank a few people.

A big thanks to my supervisor Kristian Berland for all the help and guidance with this master's thesis. His interest and knowledge in the field has been inspiring and he has provided a constant stream of insights, answers, and ideas to what I can include in my thesis, throughout the entire semester. I would also like to thank my co-supervisor Rasmus André Tranås, who has helped provide necessary data, along with some much-appreciated proofreading. The other members of the project research group also deserve a thank for both social and scientific input.

Thanks to my fellow students at Environmental Physics and Renewable Energy who have accompanied me through both social life and many long hours in the classrooms of NMBU. A special thanks to students in Sangkoret Lærken who has helped me keep my grades at an acceptable level. I would also like to thank all the other student at NMBU who has contributed to making it such a great place to be a student.

Finally, I would like to thank all my friends and family who have supported me through these years, especially Arne Auen Grimenes who helped convince me to start at NMBU, and my parents who always want to get invited yet rarely have time to visit me.

Øven Andreas Grimenes
ÅS, June 2021

Abstract

Thermoelectric (TE) generators have seen a lot of renewed interest over the last years. Along with increasing computational power, the approach in the search for new TE materials has seen a shift to first principle calculations. This study employs a high-throughput-like method for first principle calculations on half-Heusler (HH) materials. Based on the high-throughput (HT) result a subgroup is then selected for volumetric band alignment (VBA). VBA approximates alloying by varying the volume of the crystal structure. Since this approximation can be performed on primitive cells it is computationally inexpensive and can be applied to higher numbers of materials than more expensive supercell calculations. By combining HT screening with VBA this study develops a way to search a large group of materials, but also optimize the thermoelectric figure of merit (ZT) by alloying. Finally, supercell calculations are performed to give an indication of the accuracy of the VBA approximation.

From the first set of calculations for 67 materials, several showed good TE properties. LaRhTe was found to have both a very low thermal conductivity and a reasonably good power factor giving it a predicted $ZT = 2.7$, for its relaxed structure. Out of the 67 materials, 11 were chosen for VBA, some based on high ZT and others based on promising features in the band structure.

The volume of the 11 materials was adjusted by changing the lattice constant up and down 5% and new first principle calculations were performed. The VBA showed promising results for some compounds. As the volume changed, materials such as LiZnSb and LaPtSb had an impressive increase in ZT, up to as high as 3.5 for the latter. In general, the only materials that did not show an increase in ZT were materials where two or more band valleys were already well aligned. The result from VBA was attempted to be verified by supercell calculations. The unfolded band structures showed a similar trend at the Γ-point compared to the VBA calculations, but the results were inconclusive.

Sammendrag

Termoelektriske (TE) generatorer har sett økende interesse de siste årene. Med økende datakraft har tilnærmingen i søket etter TE-materialer skiftet mot førsteprinsipp beregninger. Denne studien benyttes en høy-gjennomstrømsmetode for førsteprinsipp beregninger på halv-Heusler-materialer. Basert på resultatene ble en undergruppe valgt til volumetrisk bånd-tilpasning (VBA). VBA approksimerer legeringer ved å variere volumet til krystall-strukturen. Siden denne approksimasjonen kan utføres på primitive celler er den beregnings-messig billig og kan bli utført på høyere antall materialer enn dyrere supercelleberegninger. Ved å kombinere disse to metodene utvikler denne studien en måte å søke gjennom et stort antall materialer og samtidig optimere det termoelektriske verdien (ZT) ved legering. Til slutt ble supercelle-beregninger utført for å gi en indikasjon på nøyaktigheten til VBA-approksimasjonen.

Fra de første beregningene på 67 materialer viste flere gode TE-egenskaper. LaRhTe ble funnet til å ha både lav termisk ledningsevne og høy effektfaktor, noe som resulterer i en beregenet ZT på 2.7 for den relakserte krystallstrukturen. Av de 67 materialene ble 11 valgt til VBA, noen basert på høy ZT, andre på grunn av lovende trekk i båndstrukturen.

Volumet til de 11 utvalgte materialene ble endre ved å justere opp og ned gitterkonstanten 5%, så ble nye førsteprinsippsberegninger utført. Den volumetriske bånd-tilpasningen viste lovende resultater. LaPtSb og LiZnSb viste begge stor økning i ZT, opp til så mye som 3.5 for LaPtSb. Generelt viste alle materialer en økning i ZT med mindre to eller flere bånd allerede var godt tilpasset i energinivå. Resultatene fra VBA ble forsøkt verifisert med supercelleberegninger. Båndstrukturene viste likhetstrekk til VBA-beregningene rund Γ-punktet, men dette resultatet ble ansett til å være usikkert.

Contents

Nomenclature

κ_ℓ	Lattice thermal conductivity
κ_e	Electron thermal conductivity
σ	Electrical conductivity
PF	Power factor
S	Seebeck coefficient
T	Temperature
ZT	Thermoelectric figure of merit
BTE	Boltzmann's Transport Equation
DFT	Density functional theory
DOS	Density of states
HH	half-Heusler
HT	High-throughput
LDOS	Local density of states
VBA	Volumetric band alignment

Chapter 1

Introduction

Over the last century, there has been a manyfold increase in global energy consumption[1]. Industrialized agriculture, heavy industry, mass production of goods, widespread travel, and transportation all rely on the availability of energy. Such abundant energy usage has led to a sharp increase in the living standard and economic growth in most countries in the world. Unfortunately, a vast majority of the energy consumed comes from non-renewable fossil fuels, as much as 84.3% in 2019[1]. The accompanying release of greenhouse gasses, such as CO_2, has caused an increase in the global temperature and climate change[2]. Still, global energy consumption is expected to continue to rise as more countries develop and increase their standard of living. To meet the increasing energy demand in a climate friendly way, new sustainable energy solutions are required.

Much progress is being made in the field of renewable energy, but as of 2019, only 11.4% of global energy production came from renewable sources[1]. To help reduce demand for renewable energy we should try to better use the energy we currently produce and reduce waste. It is estimated that around 36% of global primary energy consumption is lost as heat transfer alone with combustion, electrical friction, and other factors also contributing to generating waste heat[3]. Other estimates suggest that as much as 245 EJ of energy was lost as waste heat in 2012[4]. While waste heat is often difficult to harvest in an economically viable way, the potential is enormous should it be possible.

One way to convert heat to a more useful form of energy is with thermoelectric (TE) generators. A TE material is a material that can produce electricity from a temperature difference. This technology can be scaled up or down depending on the application and optimized for different temperatures making it useful in many areas, from space probes[5] to wearable devices that produce electricity from body heat[6]. The lack of moving parts and stable working conditions ensures that most TE generators can produce electricity for long periods of time without service. With

the possibility to harvest "free" waste energy and flexibility in applications, one would think TE generators were in use everywhere.

Unfortunately, the efficiency of TE generators is rather low. Since the efficiency depends on the working conditions it is often more useful to define a TE material by a unitless property called the figure of merit (ZT), defined in eq. 2.1 and related to efficiency by eq. 2.3. For commercially available TE generators the value of ZT is below 1, which under good working conditions can results in an efficiency around 5-10%[7], depending on the temperature difference. Even under optimal laboratory conditions for prototype materials few reach a higher ZT than 2[8][9]. Due to the low efficiency, TE generators are generally not economically viable and are only used in niche applications where other methods of supplying electricity would be difficult or expensive. An increase in ZT to 3 or more could greatly increase how frequently and in what applications TE generators are used.

In recent years progress in increasing ZT has been made and research on TE materials has seen a renewed interest[8][10][11]. The effort put into finding new compounds and alloys with high ZT has increased greatly, but the vast amount of possible materials makes it a difficult task. First principle calculations are a good way to quickly get estimates of the properties of a material, these methods can be implemented in high throughput surveys that search a great span of materials. Compared to only using experimental methods, the cost, time and amount of equipment necessary to search for better TE materials can be greatly reduced. The most promising materials can then be investigated in more detail and ultimately synthesized for testing. Since first principle calculations only give estimates of properties the final say in the actual properties of a bulk material will always have to come from an experimental approach.

There are a few different first principal approaches to finding better TE materials, mostly divided into three groups, sometimes also combined with experimental verification. The first is to perform high-throughput surveys, searching potentially large groups of materials. Some earlier high-throughput work has focused on silicides[12], half-Heusler materials[13], or other groups materials[14]. While the benefits of being able to screen many materials are obvious, this approach is prone to dismissing materials that have a low ZT in their pure forms, but could have great potential as part of an alloy. The second approach is trying to optimize one or a few specific materials by alloying. Alloys involving BiTe[15], PbTe[5][16] or SiGe[17] have been among the most common to study, but also many half-Heusler materials containing alloys of ZrNiSn and HfCoSb[18][19][20] have recently been shown more interest. The third approach is similar to the second, but the focus is now shifted to the nanostructure of the material. This approach has gained more traction in the last years as the understanding of the effects of different nanostructures and computational power has increased[10][21][11]. Of course, many studies use methods where these approaches overlap, that will also be the case in this master's thesis.

The idea of this master's thesis is to combine high-throughput methods with an approximation of alloying by changing the volume[22], known as volumetric band

alignment (VBA). With this approach, a screening is performed, then a set of materials that will be investigated more thoroughly is chosen. How the TE properties change under alloying can with this approximation then be calculated in a computationally inexpensive way. This allows for a wide study that searches for high ZT both in a large group of materials, and their alloys. My main goals in this master's thesis are as listed below:

- Explore the band structures and TE properties of many materials by using a high-throughput method.
- Select a subgroup of promising materials of which alloying is approximated through VBA.

My sub-goals for this master's thesis are as follows:

- Exploring what features of band structures that result in high-performance TE materials.
- To verify the results of VBA by performing supercell calculations.
- Contribute to general knowledge in the field of thermoelectric materials.

In the next chapter the underlying theory of thermoelectricity, Boltzmann's transport equation, and density functional theory are presented. These are topics essential to understanding how first principle calculations are performed, what electron transport properties are, and how these can be calculated. After that, the methods that are used to achieve my goals are explained and some details about the calculations are presented. The results will then be presented in a series of figures and finally discussed.

Chapter 2

Theory

To understand how a thermoelectric (TE) generator works it is first necessary to understand how and why some materials exhibit TE properties. This theory section will first present the TE figure of merit (ZT), a unitless measure used to characterize TE materials. Then, each of the electron transport properties that ZT consists of are explained. Further, the equation that is used to calculate these properties, the Boltzmann's transport equation (BTE), will be derived and an approximated solution will be found. Lastly, a brief introduction to the density functional theory, the basis of the first principle calculations, will be presented.

2.1 Thermoelectricity

2.1.1 Figure of merit, ZT

When describing how any generator should perform, it is often difficult to accurately predict what the actual working efficiency will be. This is especially true for generators that rely on temperature difference as the efficiency will greatly depend on the working conditions. Because of this TE materials are often described by a unitless figure of merit defined as[23]:

$$ZT = \frac{S^2 \sigma T}{\kappa_{el} + \kappa_{\ell}}, \tag{2.1}$$

where S is the Seebeck coefficient, σ is conductivity, T is temperature, κ_{el} is electron thermal conductivity and κ_{ℓ} is the lattice thermal conductivity. To have a high ZT, a material needs low thermal transport and high electron transport, the latter is usually

referred to as the power factor (PF), defined as

$$PF = S^2\sigma. \tag{2.2}$$

With ZT the maximum efficiency can be calculated if the temperature of both the hot (T_{hot}) and the cold (T_{cold}) side is know:

$$\eta = \frac{T_{\text{hot}} - T_{\text{cold}}}{T_{\text{hot}}} \left(\frac{\sqrt{1 + ZT_{\text{m}}} - 1}{\sqrt{1 + ZT_{\text{m}} + \frac{T_{\text{cold}}}{T_{\text{hot}}}}} \right), \tag{2.3}$$

where ZT_{m} is the average ZT between T_{hot} and T_{cold}. To understand how a thermoelectric material can generate electricity, it is first important to understand the different material properties that ZT consists of.

2.1.2 Seebeck coefficient, S

In 1794 the physicist Allessandro Volta observed that an iron rod with one hot and one cold end would also have a voltage difference[24]. This effect is now known as the Seebeck effect and is measured as voltage difference over temperature difference, $\Delta V/\Delta T$. Since that this measure, the Seebeck coefficient, describes a material's ability to create a voltage difference, it is arguably the most central of all the properties that go into ZT. One way to understand how a material can build up a voltage like this is by looking to the Fermi-Dirac (FD) distribution of fermions[25]. FD gives the probability that an electron state is occupied, here as a function of energy,

$$f_(E) = \frac{1}{\exp\left(\frac{E - E_{\text{F}}}{k_{\text{B}}T}\right) + 1}, \tag{2.4}$$

where E_{F} is the Fermi energy and k_{B} is Boltzmann's constant. Two such functions for different temperatures are shown in Figure 2.1.a. As shown in the graphs, the hot side has more electrons in the high energy states above the Fermi energy. These electrons could occupy lower energy states on the cold side of the material even if this would lead to net negative charge on that side. The difference in the FD distribution will cause transport of electrons from the hot side to the cold. Below the Fermi energy, the cold side has more electrons and the transport will happen in the opposite direction. It is common to instead label this as transport of electron-holes. The difference between the FD functions is shown in Figure 2.1.b as Δf(E). With electron transport in both directions, why does would charge build up on one side?

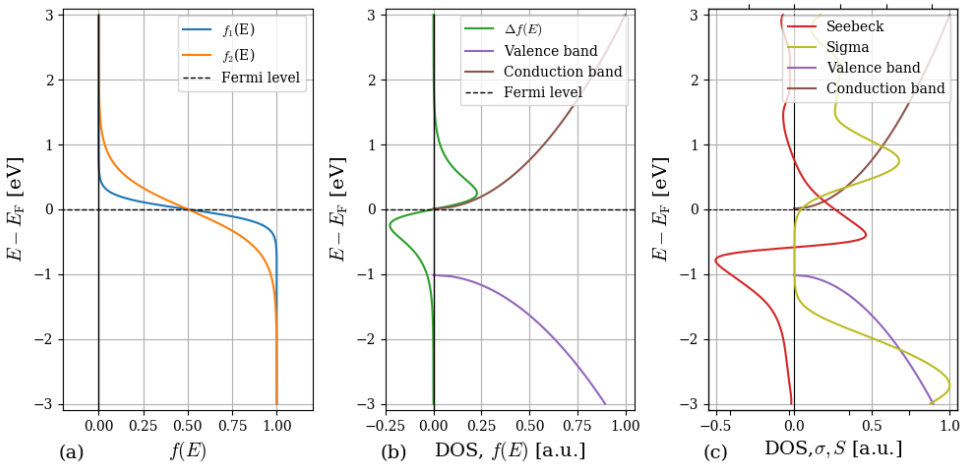

Figure 2.1: a) The Fermi-Dirac distribution at two different temperatures. b) The difference between two FD distributions together with the DOS for the valance band and the conduction band. The Fermi energy is aligned to the bottom for the conduction band in this figure. c)The Seebeck coefficient and electrical conductivity with respect to Fermi level.

In most metals, the electrons can indeed travel in both directions. This results in metals having a low Seebeck coefficient and makes them poor TE materials. However, the electron transport is not a result of the difference in Fermi-Dirac distribution alone. Figure 2.1.b shows a density of states (DOS) for the valence band and the conduction band together with $\Delta f(E)$. For the purpose of illustration, the Fermi energy is aligned with the bottom of the conduction band. While the difference in the FD function presented in the figure would predict electron transport from the cold side to the hot, there are no electron states at this energy. This leads to electrons being transported dominantly in one direction, build-up of charge, and a material with a high Seebeck coefficient. This strong dependence on the overlap of $\Delta f(E)$ and DOS means that the transport properties of a material vary with the Fermi energy. This is shown for the Seebeck coefficient and electrical conductivity in Figure 2.1.c.

Since Δf(E) overlaps with the conduction band in Figure 2.1.b this Fermi energy would result in an n-type TE material. By shifting the Fermi energy to the valence band, holes would be transported instead and result in a p-type material. Shifting the Fermi energy further into the conduction band allows for transport in both directions, making the material behave more like a metal and giving it a low Seebeck coefficient[26].

2.1.3 Electrical conductivity, σ

To maximize the electron transport and minimize resistive losses a high electrical conductivity is required, ref eq. 2.1. This can be difficult to achieve at the same time as a high Seebeck coefficient. Generally, a higher DOS at the Fermi energy results in higher conductivity. Since the DOS is low close to the band gap, getting a high conductivity requires adjusting the Fermi level well into a band. That would, on the other hand, result in a low Seebeck coefficient. Ultimately, this becomes a trade-off between conductivity and Seebeck coefficient, as shown in Figure 2.1.c.

2.1.4 Temperature

As seen in eq. 2.1, ZT increases linearly as a function of temperature. While temperature is not a material property it is still important that the TE material is stable at high temperatures to get a high ZT. This depends on the intended usage of the TE generator. If the goal is harvesting waste heat, stability at very high temperatures might not be necessary as most waste heat occurs at temperatures below 300°C[4]. The stability of different compounds at various temperatures will not be considered in this master's thesis.

2.1.5 Electron and lattice thermal conductivity

To generate as much electron transport possible for the least amount of heat, it is important that a TE material has low thermal conductivity. The thermal conductivity can be divided into two parts, the electron thermal conductivity (κ_e) and the lattice thermal conductivity (κ_ℓ). The latter is the only material property that does not depend directly on the electronic structure, but rather the vibration of the atomic nuclei in the crystal lattice. This is also the only material property that goes into the expression for ZT that will not be calculated in this master's thesis.

As electrons travel from the hot side thermal energy is absorbed by the electrons and then deposited when they reach the cold side. This effect is cannot be avoided entirely as the transport of electrons is essential. In fact, the electronic thermal conductivity is strongly tied to the electrical conductivity according to Widemann-Franz law[25]:

$$\frac{\kappa_e}{\sigma} = LT, \tag{2.5}$$

where L is the Lorenz number. The theoretical Lorenz number for metals is defined as

$$L_0 = \frac{\pi^2}{3}\left(\frac{k_\mathrm{B}}{e}\right)^2, \tag{2.6}$$

but the actual number varies in the range $1.5 - 3 \times 10^{-8}$ W/K^2 for degenerate semiconductors[27]. Again, there is a trade-off between two properties since TE material should have a high electric conductivity at the same time as a low electron thermal conductivity.

2.1.6 Fermi energy and carrier concentration

In Figure 2.1.c the Seebeck coefficient and the electrical conductivity are plotted with respect to the Fermi energy. The Fermi energy can be adjusted up or down by either n-doping or p-doping the material. Some times it is more useful to show the electron transport properties with respect to doping concentration. Figure 2.2 shows an example of the Seebeck coefficient, the power factor, the electric conductivity, and the electron thermal conductivity with respect to carrier concentration for n- and p-doping. As the figure shows, the carrier concentration grows logarithmically, making it impossible to dope the Fermi energy to arbitrary levels. The majority of figures in this master's thesis shows the transport properties and ZT with respect to Fermi energy.

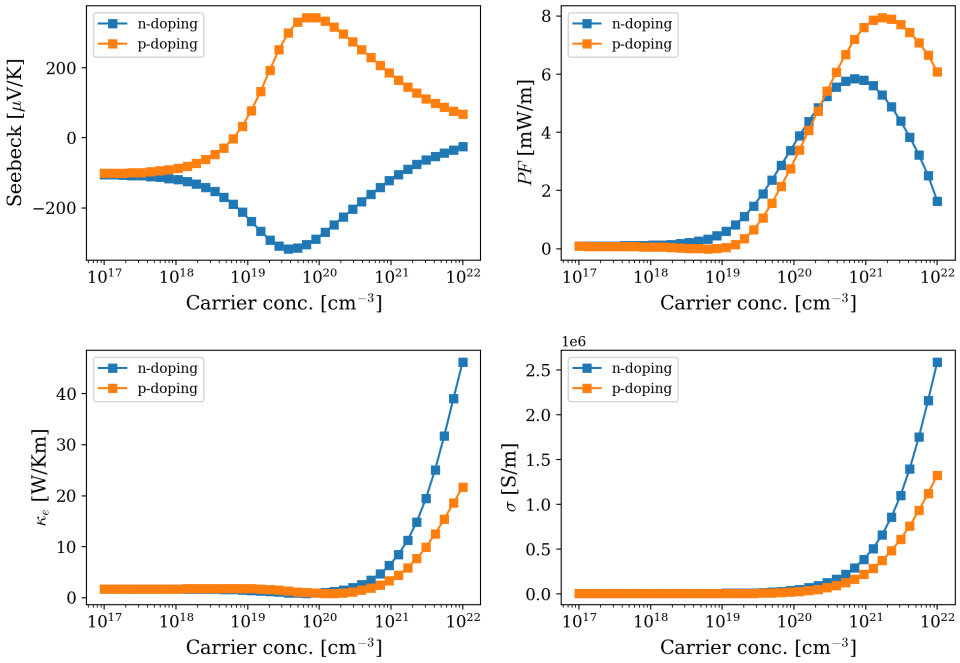

Figure 2.2: Seebeck coefficient, power factor, electric conductivity and electron thermal conductivity for n- and p-doped material.

2.1.7 Thermoelectric materials

As stated earlier, most metals are not good TE materials. Not only do they generally have a low Seebeck coefficient, but also conduct heat well. In the search for new and better TE materials, it is important to search among the right group of materials. Since a high Seebeck coefficient is dependent on having some band gap, but the electrical conductivity should not be too low, semiconductors are a natural choice. Many, though not all, semiconductors also have low thermal conductivity. This master's thesis focuses on a group of semiconductors known as half-Huesler (HH) materials. These combine the NaCl (YZ) and the Zinc-blende (XZ) crystal structure with a general formula XYZ, see Figure 2.3. HH materials have shown a wide range of interesting properties[28][29] and great potential as high efficiency TE materials[30].

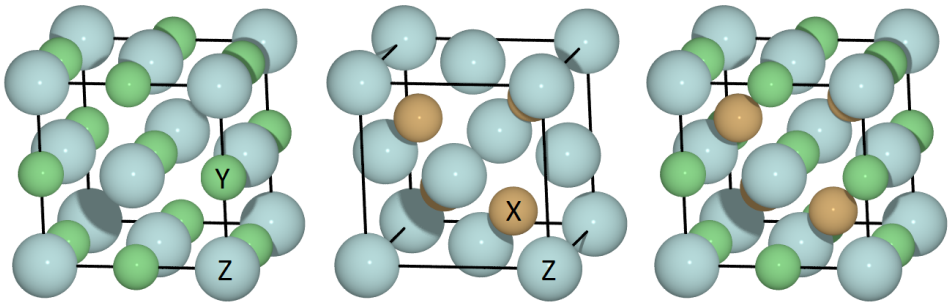

Figure 2.3: The Nacl structure (left) and zinc-blende structure (middle) combine to the half-Heusler (right).

2.2 Boltzmann's Transport Equation

2.2.1 Derivation of BTE

BTE introduces a way to calculate the electron transport properties of ZT. A more detailed derivation of BTE and the transport coefficients can be found in Lundstroms' *Fundamentals of Carrier Transport*[26]. Starting with a Fermi-Dirac distribution, now as a function of phase space and time, $f(\mathbf{r}, \mathbf{p}, t)$, describing the probability that an electron state in position $\mathbf{r}$ and momentum $\mathbf{p}$ is occupied at time t. Under the assumption that there is no magnetic field, the change in momentum is given by the gradient of the conduction band

$$\frac{d(\hbar\mathbf{k})}{dt} = -\nabla_r E_c(\mathbf{r}) = -q\mathbf{E}(\mathbf{r}), \tag{2.7}$$

$$\hbar\mathbf{k}(t) = \hbar\mathbf{k}(0) + \int_0^t -q\mathbf{E}(t')dt'. \tag{2.8}$$

Here, $\hbar$ is the reduced Plank's constant, ∇_r is the gradient in real space, E_c is the energy of the conduction band and q is the elementary charge. The velocity, and consequently the change in position, are given by

$$\mathbf{v}(t) = \frac{1}{\hbar}\nabla_k E[\mathbf{k}(t)], \tag{2.9}$$

$$\mathbf{r}(t) = \mathbf{r}(0) + \int_0^t \mathbf{v}(t')dt'. \tag{2.10}$$

∇_k is the gradient in reciprocal space. Also, the relation $\mathbf{p} = \hbar\mathbf{k}$ has been used. By assuming no in- or out-scattering the probability that an electron state is occupied remains constant

$$\frac{df}{dt} = \frac{\partial f}{\partial t} + \frac{\partial f}{\partial \mathbf{r}}\frac{d\mathbf{r}}{dt} + \frac{\partial f}{\partial \mathbf{p}}\frac{d\mathbf{p}}{dt} = 0 \tag{2.11}$$

$$\frac{df}{dt} = \frac{\partial f}{\partial t} + \frac{\partial f}{\partial \mathbf{r}}\mathbf{v} + \frac{\partial f}{\partial \mathbf{p}}\mathbf{F}_r = 0, \tag{2.12}$$

which can be written as

$$\frac{\partial f}{\partial t} + \mathbf{v}\cdot\nabla_r f + \mathbf{F}_e \cdot \nabla_p f = 0. \tag{2.13}$$

In- and out-scattering for other electron states is then introduced under the assumption that the scattering event only happens over a short period of time. The change in f is no longer 0,

$$\frac{df}{dt} = \tilde{C}f. \tag{2.14}$$

$\tilde{C}$ is the scattering operator and can under the relaxation time approximation (RTA) be defined as

$$\tilde{C}f = -\left(\frac{f(\mathbf{p}) - f_0(\mathbf{p})}{\tau_m}\right) = -\frac{\delta f(\mathbf{p})}{\tau_m}, \tag{2.15}$$

where τ_m the characteristic time and turns out to be the momentum relaxation time. Solving this equation for $f(\mathbf{p})$ will show that under RTA any perturbation of the system will relax back to equilibrium by $\exp(-t/\tau_m)$. We can now assume any that any deviation from equilibrium, δf, will be small compared to the equilibrium distribution, f_0, and approximate

$$\nabla_r f = \nabla_r(f_0 + \delta f) \approx \nabla_r f_0 \tag{2.16}$$

$$\nabla_p f = \nabla_p(f_0 + \delta f) \approx \nabla_p f_0. \tag{2.17}$$

By combining the left hand side of eq. 2.13 with the right hand side of eq. 2.15, using eq. 2.16 and 2.17 and solve for δf we get

$$\delta f = -\tau_m \mathbf{v}\cdot\nabla_r f_0 + q\tau_m \mathbf{E}\cdot\nabla_p f_0, \tag{2.18}$$

with

$$f_0 = \frac{1}{1+e^{\Theta}}, \quad \Theta = \frac{E_c(\mathbf{r}) + E(\mathbf{p}) - E_{\mathrm{F}}}{k_{\mathrm{B}}T}. \tag{2.19}$$

By solving $\nabla_r f_0$ and $\nabla_p f_0$ eq.2.18 will take the form

$$\delta f = \tau_m \left(-\frac{\partial f_0}{\partial E} \right) \mathbf{v} \{ -\nabla_r E_\mathrm{F} + T[E_c + E(\mathbf{p}) - E_\mathrm{F}] \nabla \frac{1}{T} \}, \tag{2.20}$$

often shortened by introducing a force factor,

$$\mathcal{F} = -\nabla_r E_\mathrm{F} + T[E_c + E(\mathbf{p}) - E_\mathrm{F}] \nabla \frac{1}{T} \tag{2.21}$$

so that

$$\delta f = \tau_m \left(-\frac{\partial f_0}{\partial E} \right) \mathbf{v} \cdot \mathcal{F}, \tag{2.22}$$

a solution Boltzmann transport equation. Eq. 2.20 shows that there are two forces that can push f_0 away from equilibrium, which will cause current in a circuit. First, there is the term $\nabla_r E_\mathrm{F}$, this would be a change in the Fermi energy, like from an externally applied voltage. Second, there is the term $\nabla_r 1/T$, the gradient of the inverse of temperature.

2.2.2 The coupled current equations

Different properties of a material can be found by performing different summations over momentum space involving eq. 2.22. By summing over all current densities or energy densities

$$\mathbf{J}(\mathbf{r}) = \sum_{\mathbf{p}} \frac{-q\mathbf{v}(\mathbf{p})}{\Omega} \delta f(\mathbf{r}, \mathbf{p}), \tag{2.23}$$

$$\mathbf{J}_Q(\mathbf{r}) = \sum_{\mathbf{p}} \frac{E(\mathbf{p})\mathbf{v}(\mathbf{p})}{\Omega} \delta f(\mathbf{r}, \mathbf{p}), \tag{2.24}$$

giving the current density and the electron thermal current density. Here, Ω is volume and the energy is redefined as $E(\mathbf{p}) = E_c(\mathbf{r}) + E(\mathbf{p}) - E_\mathrm{F}$. Combining these equations with eq. 2.22 gives

$$\mathbf{J}(\mathbf{r}) = \frac{-q}{\Omega} \sum_{\mathbf{p}} \mathbf{v}(\mathbf{v} \cdot \mathcal{F}) \tau_m \left(-\frac{\partial f_0}{\partial E} \right), \tag{2.25}$$

$$\mathbf{J}_Q(\mathbf{r}) = \frac{1}{\Omega} \sum_{\mathbf{p}} (E_c(\mathbf{r}) + E(\mathbf{p}) - E_\mathrm{F})(\mathbf{v} \cdot \mathcal{F}) \tau_m \left(-\frac{\partial f_0}{\partial E} \right), \tag{2.26}$$

Solving the summation over $\mathbf{p}$ gives

$$\mathbf{J} = \sigma \nabla_r \frac{E_\mathrm{F}}{q} + \sigma S \nabla_r T, \tag{2.27}$$

$$\mathbf{J}_Q = \Pi J - \kappa \nabla_r T, \tag{2.28}$$

where σ is the electrical conductivity and S is the Seebeck coefficient, Π is the Peltier coefficient and κ is the thermal conductivity, the sum of κ_e and κ_ℓ.

2.2.3 Generalized transport coefficients

By rearranging the coupled current equations for the zero electric current and the zero temperature gradient situations, expressions can be derived for all the electron transport coefficients, σ, S, Π and κ_e. It turns out that these coefficients can be expressed in terms of a generalized transport coefficient. First, the transport distribution is defined as

$$\sigma(E) = \int \sum_b \mathbf{v}_b \mathbf{v}_b \tau_m \delta(E - E_\mathrm{F}) \frac{d\mathbf{k}}{8\pi^3}. \tag{2.29}$$

Note that this equation is expressed as an integral of $\mathbf{k}$-space rather than a sum. The subscript b runs over all the energy bands and the part $\delta(E - E_\mathrm{F})$ comes for the DOS, defined as

$$n(E) = \int \sum_b \delta(E - E_\mathrm{F}) \frac{d\mathbf{k}}{8\pi^3}. \tag{2.30}$$

Now, the generalized transport coefficients can be defined with transport distribution and the solution to BTE, eq. 2.22, as

$$\mathcal{L}^{(\alpha)} = q^2 \int \sigma(E)(E - E_\mathrm{F})^\alpha \left(-\frac{\partial f_0}{\partial E} \right) dE \tag{2.31}$$

The electrical conductivity, Seebeck coefficient, Peltier coeficcient and electron thermal conductivity can now be defined as

$$\sigma = \mathcal{L}^{(0)} \tag{2.32}$$

$$S = \frac{\mathcal{L}^{(1)}}{qT\mathcal{L}^{(0)}} \tag{2.33}$$

$$\Pi = \frac{\mathcal{L}^{(1)}}{q\mathcal{L}^{(0)}} \tag{2.34}$$

$$\kappa_e = \frac{1}{q^2 T} \left[\frac{(\mathcal{L}^{(1)})^2}{\mathcal{L}^{(0)}} - \mathcal{L}^{(2)} \right]. \tag{2.35}$$

The electron thermal conductivity has two terms since it is found by defining the zero electric current electron conductivity minus a correction term

$$\kappa_e = \kappa_0 - T\sigma S^2. \tag{2.36}$$

All the expressions above can be evaluated by software such as BoltzTraP2 based on the result of first principle calculations[31].

2.3 Density Functional Theory

This section of the theory will first focus on the Scrödinger equation by trying to simplify it. Then, the Hohenberg-Khon theorems of density functional theory (DFT) is presented. These two will then be combined in the Kohn-Sham equations into modern DFT. This introduction to DFT is based on *Brief Introduction to the Density Functional Theory* by Clas Persson[32].

2.3.1 Schrödinger equation

Throughout the last century, the discovery of quantum mechanics (QM) has laid the foundation for a large portion of the progress in modern science. From material science to chemistry to particle physics, all can trace connections back to QM. Most prominent, the Schrödinger equation (SE)

$$H\Psi = E\Psi, \tag{2.37}$$

which provides a way to calculate the exact properties of any non-relativistic system of particles, in theory[33]. For a many-particle system, the equation quickly becomes more complicated, even in its time-independent form. For a N_e,N_n electron, nucleus many-particle wave-function written as

$$\Psi^{en}(\{\mathbf{r};\mathbf{R}\}) \equiv \Psi^{en}(\mathrm{r}_1, \mathbf{r}_2, ..., \mathbf{r}_{N_e}, \mathbf{R}_1, \mathbf{R}_2, ..., \mathbf{R}_{N_n}), \tag{2.38}$$

where $\mathbf{r}_i$ describes the coordinates of the i:th electron and $\mathbf{R}_j$ describes the coordinates of the j:th nucleus. The Hamiltonian for such a many-particle system would be

$$H^{en} = -\sum_i^{N_e} \frac{\hbar^2\nabla_i^2}{2m_e} - \sum_j^{N_n} \frac{\hbar^2\nabla_j^2}{2m_n} + \sum_{i<i'}^{N_e} \frac{q^2}{|\mathbf{r}-\mathbf{r}'|} + \sum_{j<j'}^{N_n} \frac{q^2 Z_j Z_{j'}}{|\mathbf{R}-\mathbf{R}'|} - \sum_i^{N_e}\sum_j^{N_n} \frac{q^2 Z_j}{|\mathbf{r}-\mathbf{R}|}. \tag{2.39}$$

The five terms of the Hamiltonian are as follows:

$T_e = -\sum_i^{N_e} \frac{\hbar^2\nabla_i^2}{2m_e}$, the kinetic energy of electrons

$T_n = -\sum_j^{N_n} \frac{\hbar^2\nabla_j^2}{2m_n}$, the kinetic energy of the nuclei

$U_{ee} = \sum_{i<i'}^{N_e} \frac{q^2}{|\mathbf{r}-\mathbf{r}'|}$, the repulsive electron-electron coulomb interaction

$U_{nn} = \sum_{j<j'}^{N_n} \frac{q^2 Z_j Z_{j'}}{|\mathbf{R}-\mathbf{R}'|}$, the repulsive nucleus-nucleus coulomb interaction

$U_{en} = -\sum_i^{N_e} \sum_j^{N_n} \frac{q^2 Z_j}{|\mathbf{r}-\mathbf{R}|}$, the attractive electron-nuclei coulomb interaction.

Note that ∇_i and ∇_j denote the gradient in the coordinates of the i:th electron and j:th nucleus. Similarly, both operators and wave functions are labeled by e or n for electrons or nuclei respectively.

To simplify the problem of solving SE a logical step is separating the electronic part and the nuclei part of the eigenfunction. By assuming the nuclei are near point-like charges with a mass much larger than the electrons it can generally be assumed that any movement of the nuclei will cause a near instant reconfiguration of the electrons. This is known as the Born-Oppenheimer approximation (BOA). Now, the nuclei eigenfunction (Θ) is independent of the position of the electrons, but the electron eigenfunction (Ψ) still depend on the position of the nuclei, $\Psi^{en}(\mathbf{r}, \mathbf{R}) = \Psi(\mathbf{r}, \mathbf{R})\Theta(\mathbf{R})$. Under this approximation, we can solve the two parts separately. Better yet, under BOA the nuclei kinetic energy, T_n, isn't of any interest, and the nucleus-nucleus coulomb interaction is easily calculated for point-like charges this interaction is usually included in the electronic Hamiltonian. Having now included every meaningful term in the electronic Hamiltonian we can find the total energy without solving the nucleus eigenfunction.

While much progress has been made, a large problem still remains with SE due to the potentially high number of electrons in a system. Firstly, the electronic eigenfunction is a function for $3N_e$ variables. For a single iron atom, this would be 78 variables. Secondly, there is the electron-electron interaction term of the Hamiltonian. Since every electron interacts with each other, this scales very quickly and becomes impossible to solve for anything but the smallest of systems. One way of simplifying this problem is to assume that the electronic eigenfunction can be described by independent single-electron wave functions,

$$\Psi(\mathbf{r}_1, \mathbf{r}_2, ..., \mathbf{r}_{N_e}) = \psi_1(r_1)\psi_2(r_2)...\psi_{N_e}(\mathbf{r}_{N_e}). \tag{2.40}$$

This is known as the Hartree approximation[34]. One issue with this approximation is that it does not require the electron wave function to be anti-symmetric. This is improved upon by what is called the Hartree-Fock approximation[35] which describes the electronic wave function with a Slater determinant

$$\Psi = \frac{1}{\sqrt{N_e!}} \det \begin{pmatrix} \psi_1(\mathbf{r}_1) & ... & \psi_{N_e}(\mathbf{r}_1) \\ \vdots & & \vdots \\ \psi_{N_e}(\mathbf{r}_1) & ... & \psi_{N_e}(\mathbf{r}_{N_e}) \end{pmatrix}. \tag{2.41}$$

This method, unlike the Hartree approximation, manages to incorporate the exchange energy of the system, a part of the electron-electron interaction that was lost when assuming independent electrons. Still, the Hartree-Fock approximation fails to incorporate the correlation energy between electrons and can still be computationally expensive to solve for larger systems.

2.3.2 Hohenberg-Kohn's theorems

Moving away from SE for a while let's take a look at a different approach to finding the properties for a quantum mechanical system. In 1964 Hohenberg and Kohn[36] stated in their first theorem that *the ground state energy from SE is a unique functional of the electron density of that system*

$$E_0 = E[n_0(\mathbf{r})], \tag{2.42}$$

where n_0 is the ground state electron density defined as

$$n_0(\mathbf{r}) = |\mathbf{\Psi}(\mathbf{r}_1, .., \mathbf{r}_n)|^2. \tag{2.43}$$

This means that the electron density uniquely determines all properties of a system, including wave function and energy. Now any problem can be reduced from $3N$ number of dimensions to a much simpler 3-dimensional problem. Unfortunately, the functional that gives the exact ground energy is not known and the theorem provides no insight into how to find the energy. To incorporate all known physics as a functional of the electron density it is imagined that the exact functional must be very complex and perhaps it never will be found. However, Hohenberg and Kohn also stated in their second theorem that *the electron density that minimizes the energy for a given functional is the correct density corresponding to the solution of SE.* If the exact functional was known one could vary the electron density, attempting to lower the resulting energy as much as possible.

This leaves us with density functional theory, a theory that states that the energy is an exact functional of the electron density, a function of 3 dimension that is easy to work with, and the variation principle to find a ground-state electron density, but no idea of what the exact functional is. On the other hand, SE allows us to calculate much of the total energy of the system by making a few approximations. These approximations, unfortunately, exclude the very important correlation and exchange energy. Modern DFT is a mix of these two approaches.

2.3.3 Kohn-Sham equations

By generating a Hartree-like electronic wave function

$$\Psi(\mathbf{r}_1, ..., \mathbf{r}_{N_e}) = \psi_1^{KS}(\mathbf{r}_1)...\psi_{N_e}^{KS}(\mathbf{r}_{N_e}) \tag{2.44}$$

some components of the total energy can be calculated along with the electron density, $n(\mathbf{r})$.

$T_s = \sum_i \int \psi_i^{KS*} \frac{-\hbar^2\nabla^2}{2m_e} \psi_i^{KS} d\mathbf{r}$, the independent electron kinetic energy

$U_{en} = \int V_{en}(\mathbf{r}) n(\mathbf{r}) d\mathbf{r}$, the electron-nuclei interaction

$U_s = \frac{1}{2}\int\int q^2 \frac{n(\mathbf{r})n(\mathbf{r}')}{|\mathbf{r}-\mathbf{r}'|} d\mathbf{r}d\mathbf{r}'$, the independent electron coulomb interaction.

Note that the nucleus-nucleus coulomb interaction has been left out here since it is generally only calculated once. The difference between the sum of these energies and the true energy is the exchange-correlation energy, $E_{xc} = (T[n] - T_s[n]) + (U_{ee}[n] - U_s[n])$. This remaining energy will be calculated as functional of the electron density. By defining the exchange-correlation potential

$$V_{xc} = \frac{\partial E_{xc}[n]}{\partial n} \tag{2.45}$$

combining these energies, we get

$$\left\{ \frac{-\hbar^2\nabla_i^2}{2m_e} + \int \frac{q^2 n(\mathbf{r}')}{|\mathbf{r}-\mathbf{r}'|} d\mathbf{r}' + V_{en}(\mathbf{r}) + V_{xc}(\mathbf{r}) \right\} \psi_i^{KS}(\mathbf{r}) = \mathcal{E}_i \psi_i^{KS}(\mathbf{r}), \tag{2.46}$$

written a little simpler as

$$\left\{ \frac{-\hbar^2\nabla_i^2}{2m_e} + V_{\mathbf{H}}(\mathbf{r}) + V_{en}(\mathbf{r}) + V_{xc}(\mathbf{r}) \right\} \psi_i^{KS}(\mathbf{r}) = \mathcal{E}_i \psi_i^{KS}(\mathbf{r}). \tag{2.47}$$

This is the Kohn-Sham single electron equation[37]. Solving a set of these eigenproblems will yield the electron energy levels.

2.3.4 Bloch's theorem

The Kohn-Sham equations showed that the total energy could be calculated from single electron Hartree-like wave functions, but made no claim on how to express these wave functions. Bloch's theorem[38] states that a solution to SE in a periodic system can be expressed as a sum of terms with the form

$$\psi_{\mathbf{k}} = \exp(i\mathbf{k}\cdot\mathbf{r}) u_{\mathbf{k}}(\mathbf{r}). \tag{2.48}$$

Here, $u(\mathbf{r})$ is a function periodic with the unit cell and $\exp(i\mathbf{k}\cdot\mathbf{r})$ is a plane wave that modulates $u(\mathbf{r})$ with a frequency depending on $\mathbf{k}$. Since $u(\mathbf{r})$ is periodic with the unit cell it can be expressed as a Fourier series of a special set of plane waves

$$u(\mathbf{r}) = \sum_{\mathbf{G}} c_{\mathbf{G}} \exp(i\mathbf{G}\cdot\mathbf{r}) \tag{2.49}$$

where $\mathbf{G}$ is any full cell translation in reciprocal space. Combining eq. 2.49 and eq. 2.48 gives

$$\psi_{\mathbf{k}} = \sum_{\mathbf{G}} c_{\mathbf{G}} \exp(i(\mathbf{k}+\mathbf{G})\cdot\mathbf{r}). \tag{2.50}$$

Like any Fourier series, this expression can be expanded infinitely, so a criterion for when to stop is necessary. Usually, this sum is truncated to only contain solutions with kinetic energy below a certain value

$$E = \frac{\hbar^2|\mathbf{k}+\mathbf{G}|^2}{2m_e} < E_{cut}. \tag{2.51}$$

This energy, E_{cut}, is known as the energy cutoff. What value chosen for energy cutoff is important to consider, as a high energy cutoff will increase the accuracy of calculation, but also increase the computational cost. Another factor that is important to the cost is the density of sampling mesh in **k**-space. Since the energy depends on **k** we would like to know the energy everywhere in the first Brillouin zone, but it is only calculated at points. Like energy cutoff, this also becomes a trade-off between accuracy and cost.

2.3.5 Exchange-correlation functionals

The exact functional neither for total ground state energy $E[n_0]$ nor the exchange-correlation energy $E_{xc}[n]$ is known. One exchange-correlation functional assumes that the energy in each point in space is equal to the energy of a homogeneous electron gas with the same density, which can be solved exactly. This is known as the local density approximation (LDA) since the energy is only a functional of the electron density at each point in space, $E_{xc}[n(\mathbf{r})]$. Many different functionals use this approximation, such as PW92[39]. For such a simple approximation it performs surprisingly well, but by including more information about the electron density further improvements can be made.

To improve on LDA the gradient of the electron density can be included, $E_{xc}[n(\mathbf{r}), \nabla n(\mathbf{r})]$. This is known as the Generalized Gradient Approximation, GGA. This class of functionals has yielded good results for large groups of materials and is among the most commonly used functionals for plane-wave DFT. A well-known example of these is the GGA functional described by Perdew, Burke, and Ernzerhof[40] know as PBE. This functional is used for all first principle calculations in this master's thesis.

Chapter 3

Method

This chapter will first cover the software used for first principle calculations, calculation of thermoelectric properties, band unfolding, and visualization in this master's thesis. Then, each of the different steps in the method used to search for better thermoelectric (TE) materials is explained in more detail. Starting with the choice of materials and initial testing, then the high-throughput survey of the band structure and figure of merit (ZT) before moving on to the volumetric band alignment (VBA) for a few select materials. Lastly, the supercell calculations that were performed to attempt to verify the results of VBA will be covered.

3.1 Software

3.1.1 VASP

For the first principle calculations in this study Vienna Ab initio Simulation Package (VASP) 5.4.4[41] with the projector augmented-wave method for pseudopotentials[42]. The generalized gradient approximation exchange-correlation functional as described by Perdew, Burke, and Ernzerhof (PBE) was used[40]. An energy cutoff of 300 eV and 48×48×48 **k**-points were used and the effect of spin-orbit coupling was included.

3.1.2 BoltzTraP2

While VASP performs the first principle calculations that provide the electron energies, other software is required to find the electron transport properties. For this the

software BoltzTraP2[31] has been used through its PYTHON interface. BoltzTraP2 uses smooth Fourier interpolation to reconstruct the full energy bands from a first principle calculation and then calculates the transport coefficients using Boltzmann's transport equation (BTE). BoltzTraP2 can also construct the band structure and the DOS from the fine **k**-point mesh, making it a useful tool for getting much information out of a single calculation even if it does require high accuracy with regards to **k**-points. For all calculations of thermoelectric properties, a constant relaxation time of $\tau_m = 10^{-14}$s was used.

3.1.3 ASE

To automate the task of setting up and initiating VASP calculations the PYTHON package Atomic Simulation Enviroment (ASE) was used[43]. Its easy to use python interface allows can create, or copy, all VASP input files and submitting the calculations through slurm-scripts[44] to the high-performance computing cluster.

3.1.4 PyProcar and Pymatgen

Two more PYTHON packages were used to extract and visualize the results. PyProcar was employed to plot the local density of state (LDOS) for each material[45] and unfolding of the supercell calculation band structures. The PYTHON package Pymatgen[46] was used to plot electron transport properties with respect to carrier concentration.

3.2 Choice of materials and initial testing

For this study, 67 HH materials all shown to likely be stable by first principle methods were chosen[47]. All the materials are listed in Table C.1. Some initial testing was then performed to make better decisions about the required numerical precision in later calculations. These calculations focused on numerical convergence and the effect of spin-orbit coupling.

3.2.1 Numerical convergence

In computational physics, the necessary accuracy of computations should be considered carefully. By increasing the energy cutoff or number of **k**-points sampled in the Brillouin zone (BZ), the accuracy of the calculation can be increased, but so does the computational cost[48]. In high throughput surveys, it is especially important to choose these parameters with care since even a small increase in computational cost

for each calculation could result in a very large overall increase. On the other hand, if the accuracy is too low the results might not reach the required accuracy. Further, which calculated properties that are converged must also be given some thought. For this master's thesis, the focus is thermoelectric properties, therefore the convergence study will focus on ZT, power factor PF, and properties related to the band structure. The values of ZT in this chapter may differ from what is presented in the results as arbitrary values for lattice thermal conductivity were used.

Energy cutoff

To find the necessary energy cutoff a series of calculations with energy cutoffs varying from 200 eV to 450 eV at 25 eV intervals were performed, with $36\times36\times$ **k**-points. For these calculations, the HH material LiZnSb was chosen because it contains Li, which has the highest pseudopotential energy of all the elements in the HH materials in this study. By choosing Li it can then be assumed that all other elements converge as fast or faster with respect to energy cutoff.

Since the transport properties of a material depend on the curvature of the band structure, showing that this curvature remains constant with increasing energy cutoff should provide a good indication of numerical convergence. While it is difficult to put a specific number on the curvature as a whole, an approximation can be made by calculating the energy difference between two high-symmetry points. In Figure 3.1.a, the change in energy difference between the Γ-point and the W-point in the valence band for each energy cutoff is shown. This means that the figure value at 250 eV is calculated as

$$\Delta E = |(E(\Gamma) - E(W))_{225eV} - (E(\Gamma) - E(W))_{250eV}| \tag{3.1}$$

for the valence band. As expected the change between each step in energy gradually decreases, however, most of the change happens before 325 eV, that is, the change going beyond 300 eV. Figure 3.1.b shows ZT with respect to Fermi energy at different energy cutoffs. It is clear from the figure that even at the lowest energy cutoff the difference to ZT is very small. Based on these results, an energy cutoff of 300 eV was chosen for all high-throughput calculations. A higher energy cutoff of 500 eV was used for relaxation of the volume of the primitive cell as changing the volume makes the plane-wave basis set incomplete and introduces Pulay stress[49].

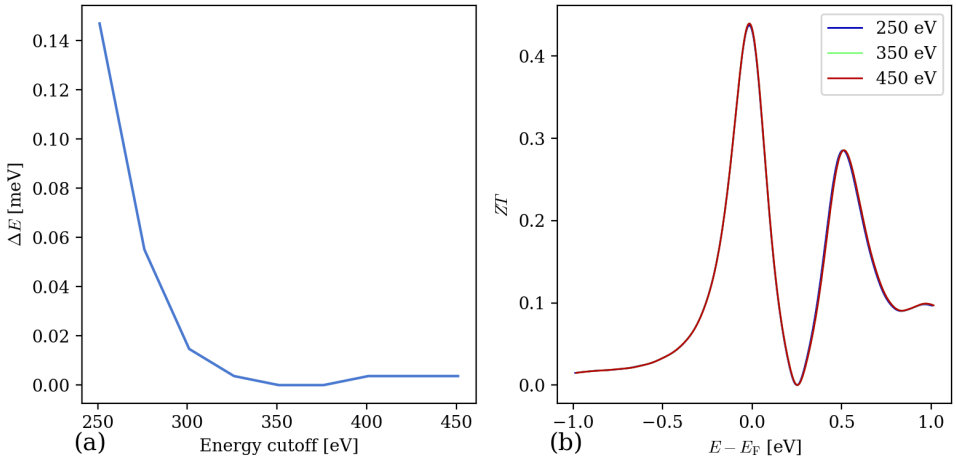

Figure 3.1: a) Change in valence band energy difference. b) Figure of merit at different energy cutoffs.

Brillouin zone sampling

BoltzTraP2 generates an very fine grid of energy values in **k**-space by interpolating between the already calculated **k**-points using smoothed Fourier interpolation[31]. The accurate calculation of transport properties still requires a significant amount of **k**-points in the first principle calculations. The calculated power factor of LiZnSb with N×N×N **k**-points ranging from 15 to 48 is shown in Figure 3.2. The figure shows that even in the range 30-40 **k**-points some parts of the power factor vary visibly. All grids of **k**-points were generated using a Γ-sentered variant of the method developed by Monkhorst and Pack[50] and with a 500 eV energy cutoff.

Figure 3.3 shows the change in band gap for each increasement in number of **k**-points. This value keeps decreasing all the way up to 45×45×45 **k**-points. Unlike for the energy cutoff, it is not given that all other compounds will converge as fast as LiZnSb. Based on these results a **k**-mesh of 48×48×48 was chosen for all primitive cell calculations. For the 2×2×2 supercells a 24×24×24 **k**-point grid was chosen to keep a similar density of **k**-points.

3.2.2 Spin-orbit coupling

Since this study includes calculations with a sizeable portion of the elements the effect of spin-orbit coupling (SOC) should be considered. Three calculations were performed to explore the effect of SOC on ZT. One without SOC, one with SOC, and one with SOC, but with the **k**-points of a calculation without SOC. The reason for the last one

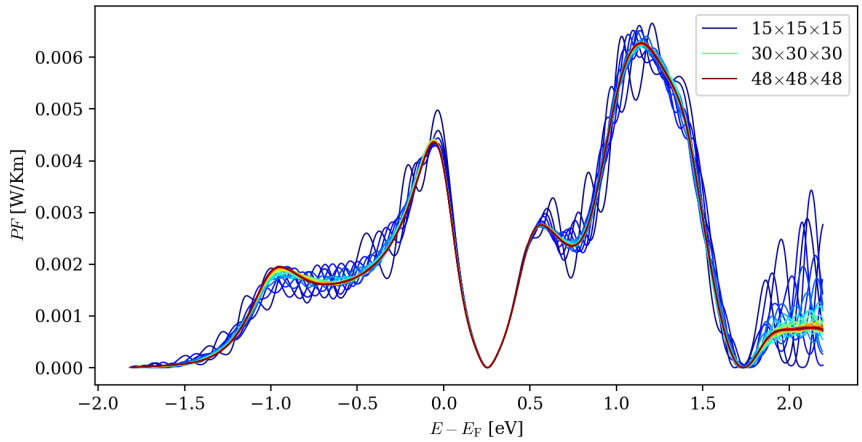

Figure 3.2: Power factor for N×N×N **k**-points ranging from 15 to 48.

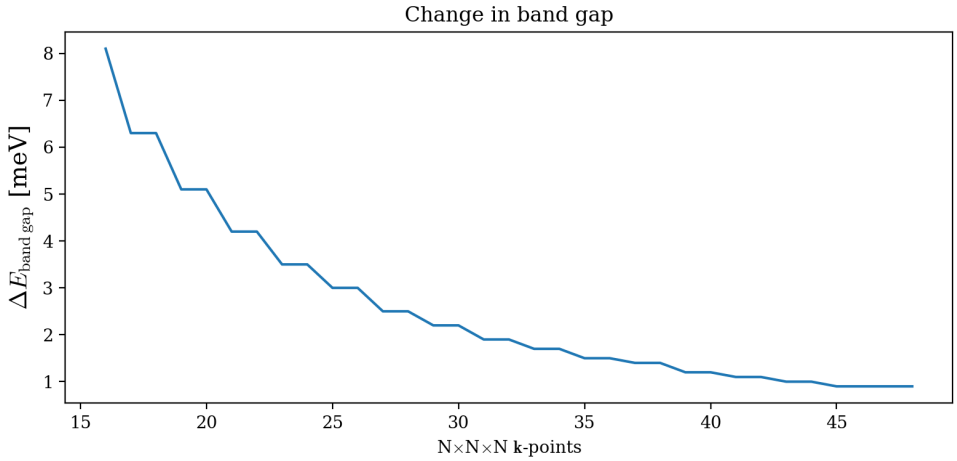

Figure 3.3: Change in band gap N×N×N **k**-points with N ranging from 15 to 48.

is that the inclusion of SOC reduces the symmetry of BZ. Because of this, the number of k-points in BZ is greatly increased along with the computational cost. Figure 3.4 shows the resulting ZT from all three calculations. As the figure shows, SOC makes a difference at some energies and should be included in later calculations. Also, the approximation of using the non-SOC **k**-points turns out to be very good. BiNiSc was chosen for these calculations since it contains Bi, which is the heaviest element in this study and should show some of the strongest SOC-effect.

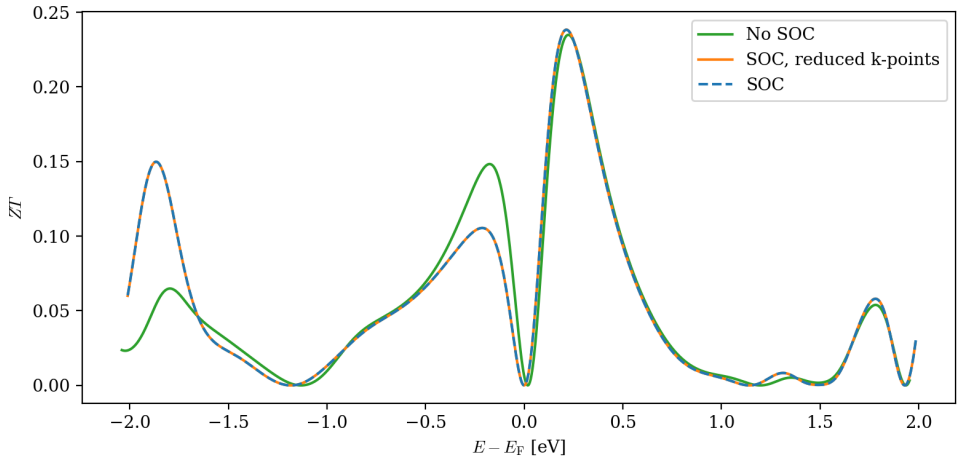

Figure 3.4: ZT calculated without spin-orbit coupling, with spin-orbit coupling and with spin-orbit coupling with reduced **k**-points.

3.3 High-throughput method

With converged values for energy cutoff and **k**-points chosen, the high-throughput calculations could begin. While performing calculations on 67 materials is not usually something seen as "high-throughput", the method of working was performed in a way that could easily be extended to a much larger number of materials. By writing PYTHON scripts using ASE the task of preparing VASP calculations has been almost fully automated. By performing calculations on primitive cells the computational cost was also kept relatively low.

Crystal structures for each material were provided by my colleague, R. A. Tranås, these were relaxed with the PBE exchange-correlation functional[40]. Based on the relaxed structures, self-consistent calculations were performed to provide the charge density of each compound. Then high **k**-point density calculations were performed to provide the local density of states, band structure, and ZT. The result can be seen in Appendix A. The results were inspected and a handful of promising materials were chosen for volumetric band alignment (VBA) based on a few criteria. Firstly, the material exhibits reasonably good thermoelectric properties in its relaxed structure. Secondly, the material has two or more valleys in the valence or conduction band that are fairly close in energy. Lastly, a few of the materials that have both of the first two properties were chosen because they belonged to a periodic group of HH materials that have many stable compounds. This increases the chance that there is another stable material with the same electron configuration that can be used as an alloy to increase or decrease the volume.

3.4 Volumetric Band Alignment

Two of the most common approaches to finding better thermoelectric materials are to either screen a large number of pure materials to look for high ZT materials or try to find the best alloy of two already good materials. Doing both at the same time is difficult because trying many different alloys for a variety of materials would require a large amount of computational power. In this master's thesis different alloys are approximated by volumetric band alignment as presented in *High-throughput exploration of alloying as design strategy for thermoelectrics* by Bhattacharya and Madsen[22].

The idea behind VBA is to align the energy level of valleys in the band structure by adjusting the volume. Aligning valence band or conduction band valleys will increase electron transport and give a better thermoelectric material. An example of how the valence band changes with the lattice constant can be seen in Figure 3.5.

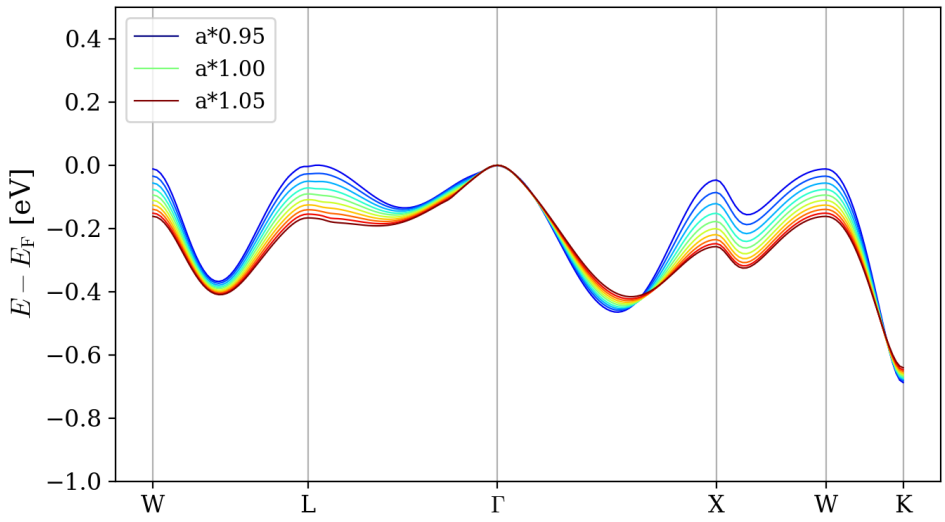

Figure 3.5: Conduction band of TaRhSb at different volumes. Notice how the band valleys align.

Freely adjusting the volume to find a good band structure might seem like an unreasonable thing to do. The justification for this approximation is that by alloying some amount of one element with another that has the same number of valence electrons the electronic properties will not change significantly around the band gap. The volume, however, will change somewhat. In this way, VBA is an approximation of alloying by only changing the volume. Since this can be done for primitive cells of a compound it provides a relatively inexpensive way to search for good thermoelectric alloys. In this master's thesis, VBA will generally refer to the process of adjusting the volume in

search of aligned band structures rather than band structures that have been aligned through volume adjustments.

3.5 Supercell verification

To more accurately describe the properties of alloys, supercell calculations can be performed. Since the number of atoms in the cell increases, so does the cost of the calculation, exactly what VBA is trying to avoid. Because of the higher cost, only a few supercell calculations were performed to verify the results of the VBA calculations, by comparing the band structures. As the size of the cell increases to contain more primitive cells the energy bands folds onto themselves making to band structure difficult to read. To recreate the primitive cell band structure PyProcar was used to unfold the band structure[45]. The supercells were created using primitive cells of the materials being alloyed with the lattice constant was set according to Vegard's law[51]

$$a = a_A(1 - x) + a_B(x), \tag{3.2}$$

where a_A and a_B are the lattice constants of the base materials and x is the relative amount of material B.

Chapter 4

Results

This chapter presents a selection of the results from the first principle and thermoelectric calculations performed in this study. Out of the 67 half-Heusler materials 11 were chosen for volumetric band alignment. The local density of states (LDOS), band structure, and figure of merit (ZT) for these materials are presented in Figure 4.1-4.3, the rest can be found in Appendix A. Due to its high ZT all the transport properties of LaRhTe are shown in Figure 4.4. Then, the power factor (PF), ZT and band structure from the VBA calculations for four materials are presented in Figure 4.5-4.8, the result from the remaining materials can be found in Appendix B. Lastly, the unfolded band structures from three supercell calculations are presented together with band structures from VBA in figure 4.9.

4.1 High-throughput calculations

In Figure 4.1, 4.2 and 4.3 the left pane shows the local density of state plotted with PyProcar[45]. The middle shows the band structure that BoltzTraP2[31] reconstructed from the interpolated **k**-pint mesh. The right pane shows ZT at 500K and 800K with respect to Fermi energy level, calculated as shown in eq. 2.1. In this section the materials that were chosen for VBA because of their interesting band structure and potentially high ZT are shown and figures for the remaining materials are shown in Appendix A.

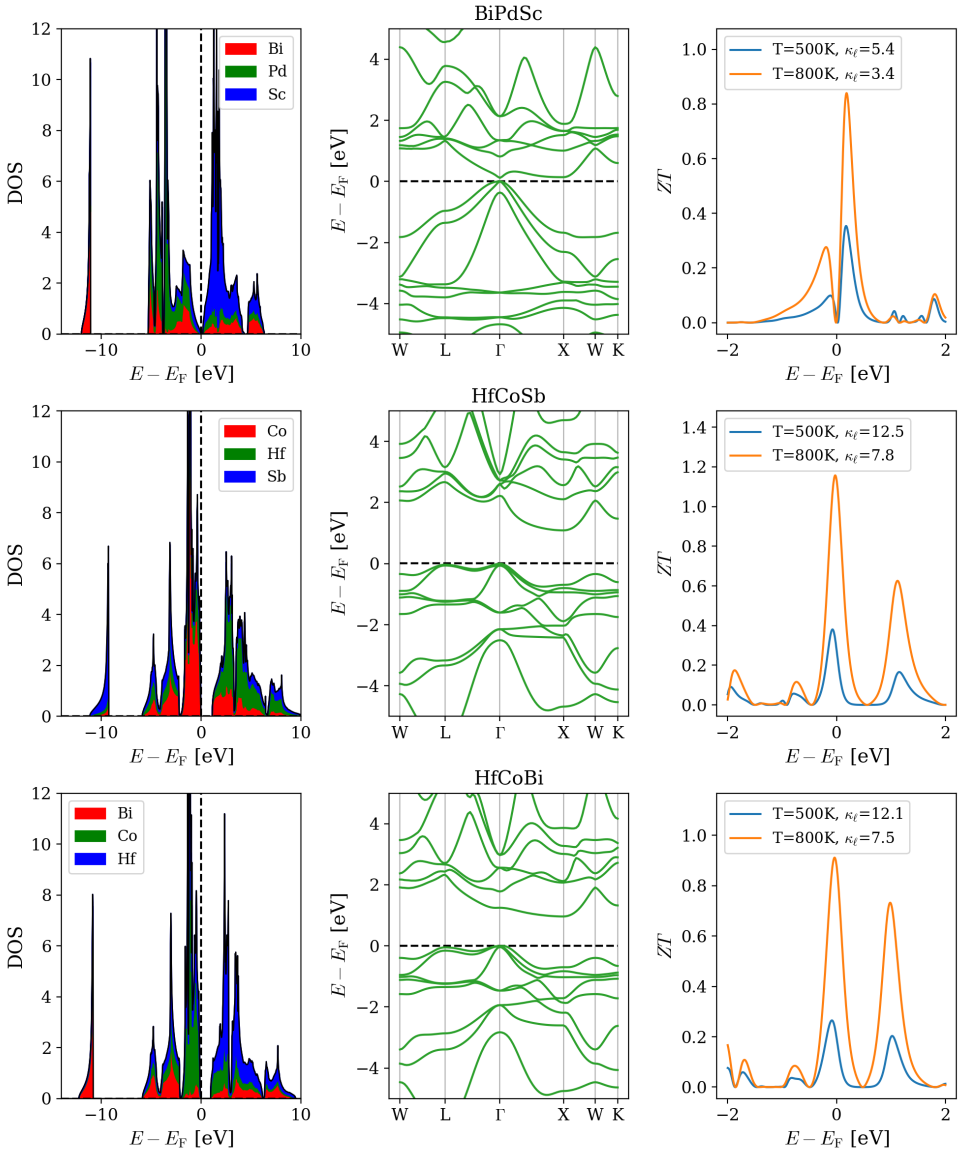

Figure 4.1: LDOS, band structure and ZT for BiPdSc, HfCoSb and HfCoBi.

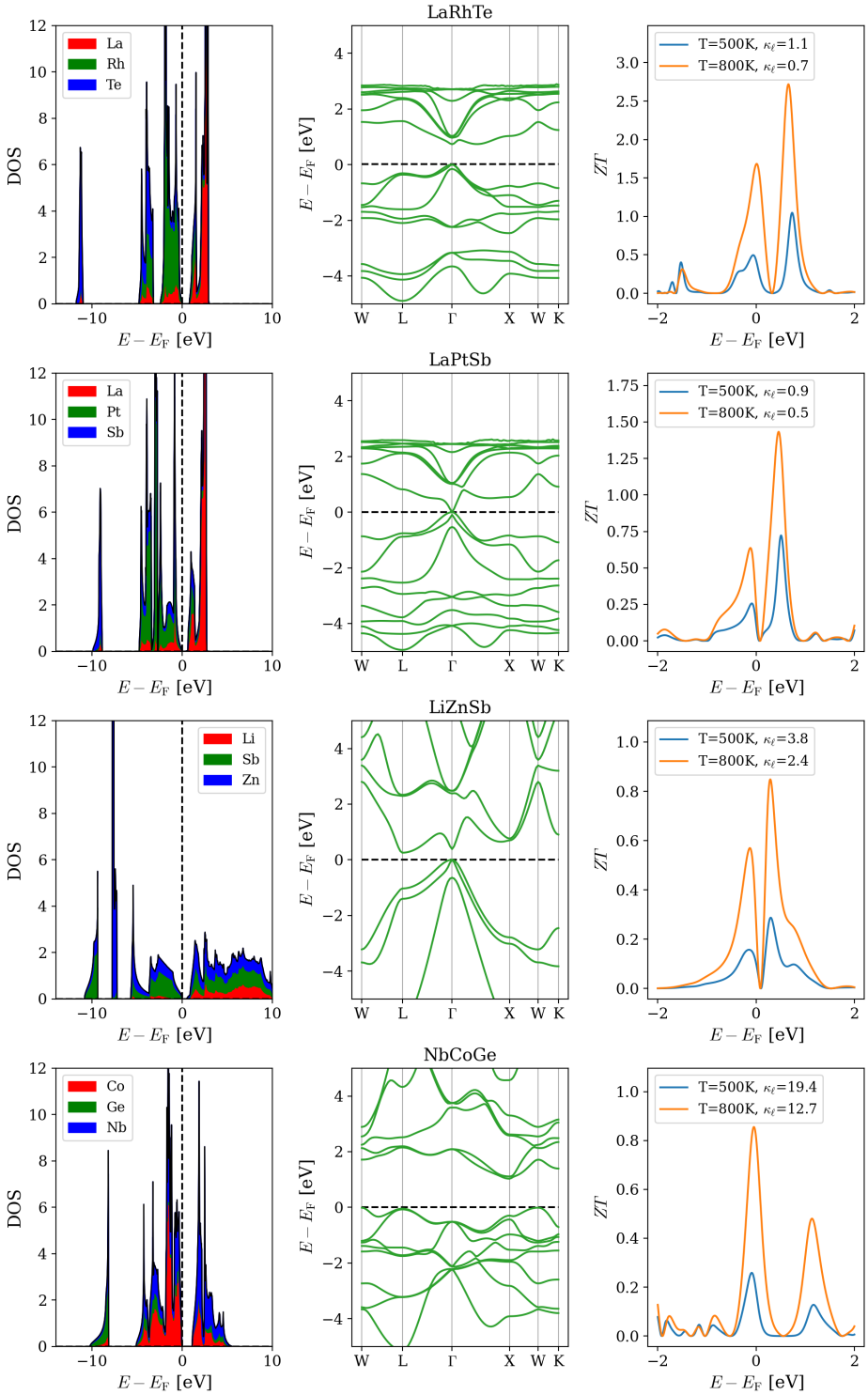

Figure 4.2: LDOS, band structure and ZT for LaRhTe, LaPtSb, LiZnSb, NbCoGe.

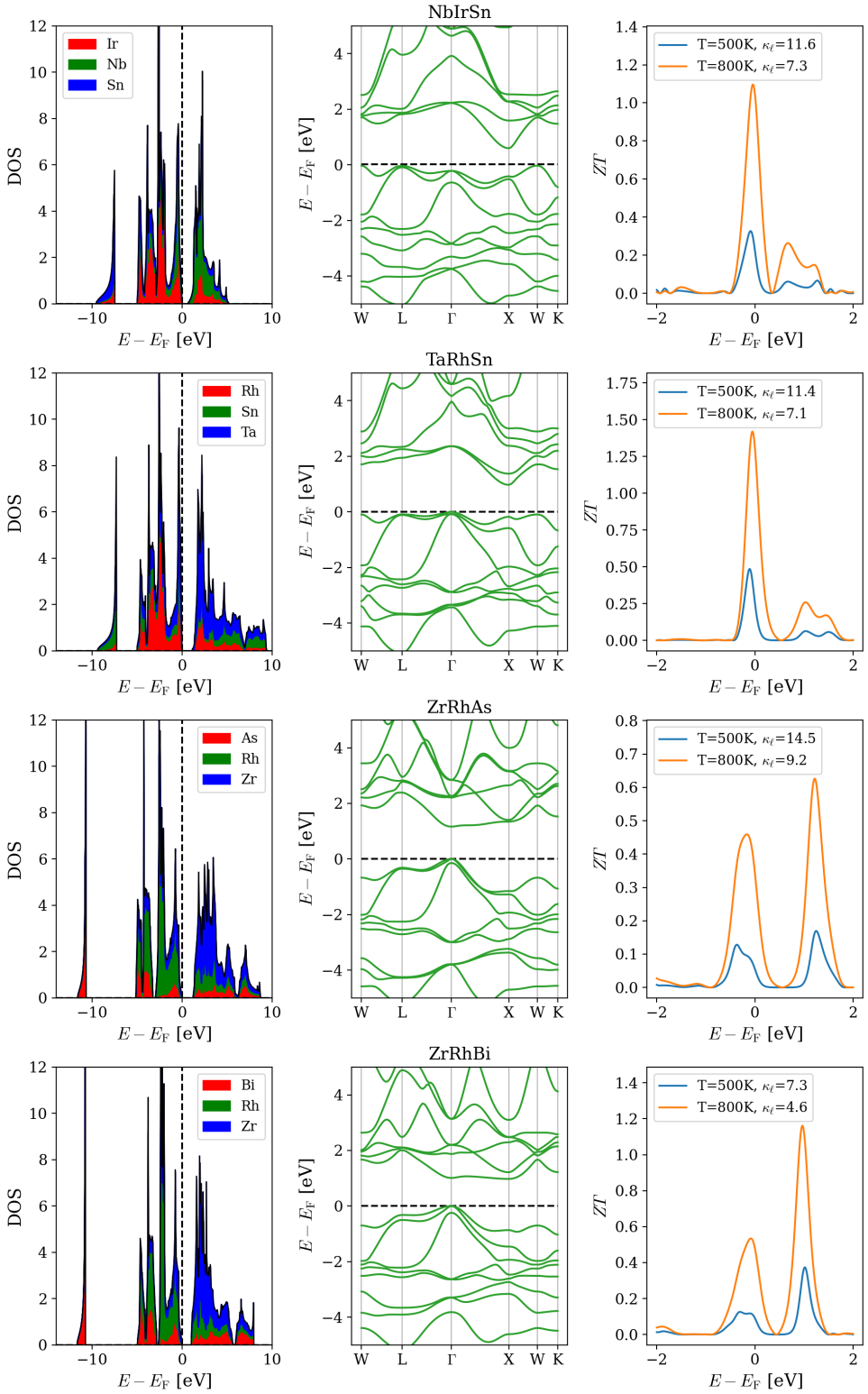

Figure 4.3: LDOS, band structure and ZT for NbIrSn, TaRSn, ZrRhAs.

BiPdSc has two well aligned band valleys in the conduction band at the Γ- and X-point, as shown in Figure 4.9. HfCoSb and HfCoBi have similar band structures, but the better aligned bands in the valence band of HfCoSb give it a higher ZT. The LDOS of HfCoSb shows that Sb contributes little to the total DOS around the band gap indicating that changing it would not result in large differences in the band structure in that area. Figure 4.2 shows that LaRhTe has $ZT = 2.7$ and a conduction band valley in between high-symmetry points. LaPtSb has a ZT of almost 1.5 despite not having a band gap. This likely means there is room for improvement. Both materials containing La shows a distortion of the band structure at around 2.5 eV, probably because of an error in the VASP pseudopotentials. LiZnSb shows two well aligned band valleys and the potential for a third to align. NbCoGe and NbIrSn in Figure 4.2 and 4.3 both have valence bands with many valleys close in energy level. Both materials also have a medium ZT despite high lattice thermal conductivity (κ_ℓ). TaRhSn has band valleys at four high-symmetry points nearly aligned and contributions from up to three energy bands. This results in a high ZT despite a somewhat high κ_ℓ. ZrRhAs and ZrRhBi show a similar LDOS and band structure, but the difference in κ_ℓ gives ZrRhBi a higher ZT.

4.2 LaRhTe

LaRhTe has calculated to have a ZT of 2.72 for optimal n-doping. Figure 4.4 shows the Seebeck coefficient (S), electrical conductivity (σ), electron thermal conductivity (κ_e), PF and ZT at 800K. At the Fermi energy of maximum ZT for n-doping LaRhTe has a Seebeck coefficient of -313 μV/K, a PF of 4.38 mW/K^{2}m, an electron thermal conductivity of 0.59 W/Km and a κ_ℓ of 0.7 W/Km. This PF is in the lower end of the materials in this study, but the very low thermal conductivity results in a high ZT.

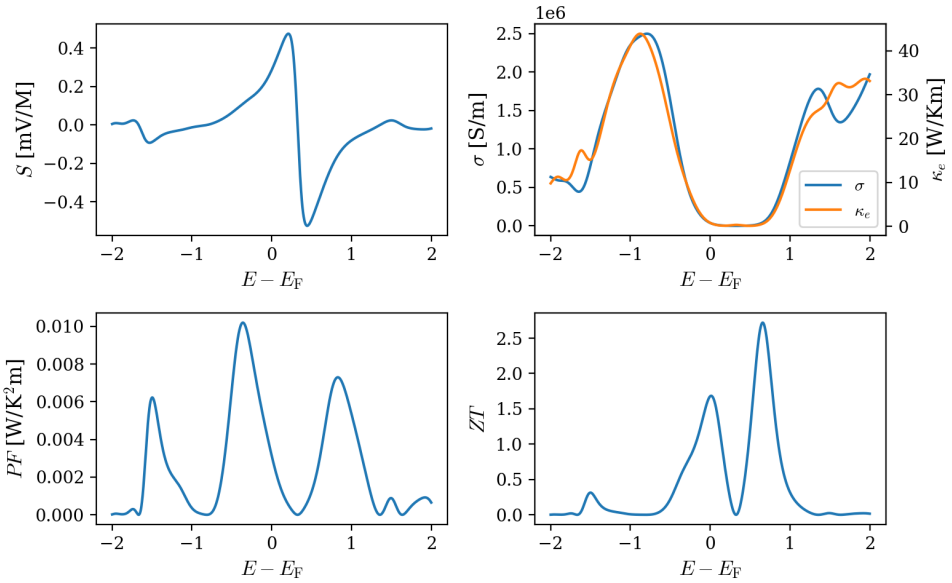

Figure 4.4: S,κ_e,κ_ℓ,PF and ZT for LaRhTe at 800K.

4.3 Volumetric Band Alignment

From the 67 HH materials, 11 were chosen for VBA. The power factor, ZT and band structures at different volumes for four of these materials are shown in figure 4.5-4.8. The results from the remaining materials are shown in Appendix B. Each figure contains results from 11 calculations where the lattice constant is scaled up and down 5% at 1% increments. The graphs are aligned at $E_F = 0$, which is set to the top of the valence band. The values of PF and ZT are calculated at 800K.

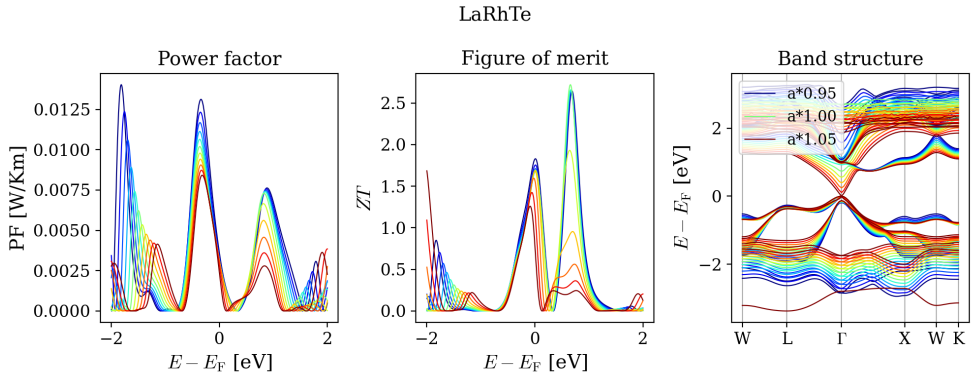

Figure 4.5: Power factor, figure of merit and band structure of LaRhTe at different volumes.

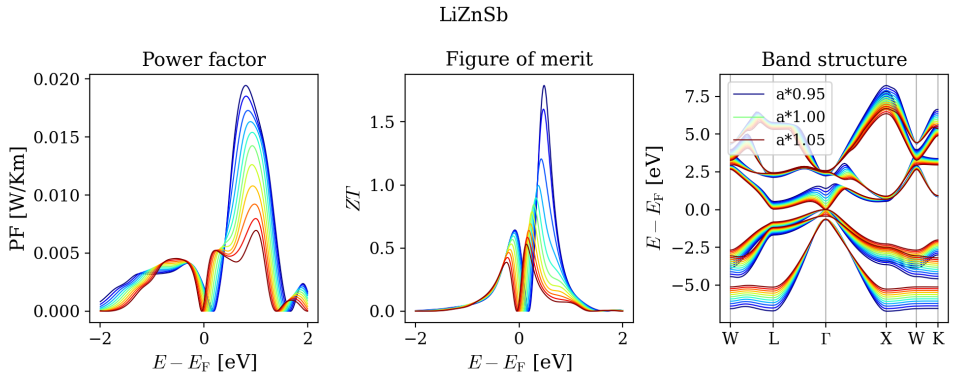

Figure 4.6: Power factor, figure of merit and band structure of LiZnSb at different volumes.

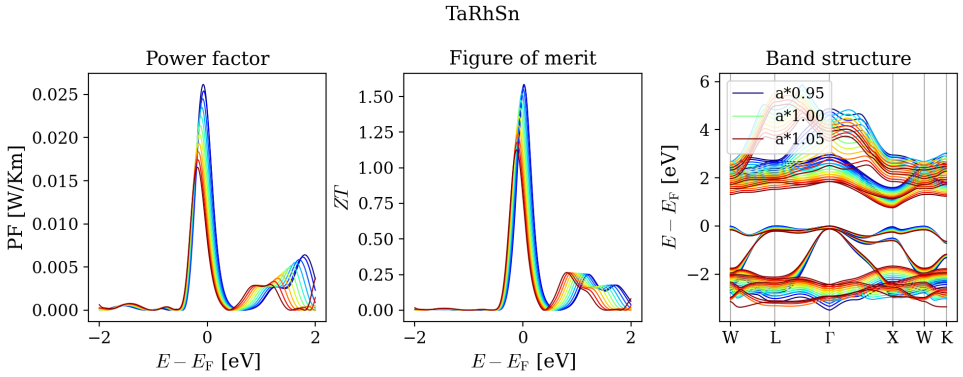

Figure 4.7: Power factor, figure of merit and band structure of TaRhSn at different volumes.

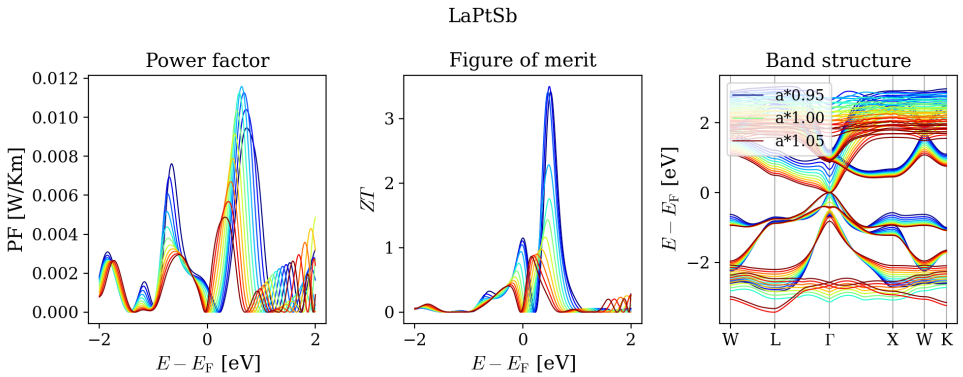

Figure 4.8: Power factor, figure of merit and band structure of LaRPtSb at different volumes.

Figure 4.5 shows that any deviation from the relaxed volume causes the valleys in the conduction band to become less aligned and a resulting decrease in ZT for an n-doped LaRhTe. For LiZnSb, shown in Figure 4.6, the L-point unaligns with the Γ-point and instead aligns with X-point. This results in a higher PF and almost a doubling ZT. TaRhSn shows a similar, but smaller increase in ZT when four of the high-symmetry points of the conduction band align under volume reduction. In some of the high-symmetry points, multiple bands align, as shown in Figure 4.7. Figure 4.8 shows that a reduction in volume raises the energy level of the Γ-point in the conduction band. This causes it to align with a wide band valley in between the Γ-point and the X-point, greatly increasing ZT to a value of 3.5.

4.4 Supercell calculations

Figure 4.9 shows the unfolded band structures of three LaPtSb supercells together with band structures from VBA calculations. The top pane contains the unfolded band structure of $La_8Pt_8Sb_8$ in blue lines and LaPtSb at the relaxed volume in red. The middle pane shows the unfolded band structure of $(LaPt)_7(ScNi)_1Sb_8$ and the primitive cell with the lattice constant is reduced by 1%. Similarly, the bottom pane shows $(LaPt)_6(ScNi)_2Sb_8$ and the primitive cell with the lattice constant reduced by 2%. The conduction band and valence band seem to change in a similar fashion in the two types of calculations. For supercells of this small size, the unfolded band structures of these alloys become distorted. This could be because the materials have too different band structures, or indicate that some error has occurred.

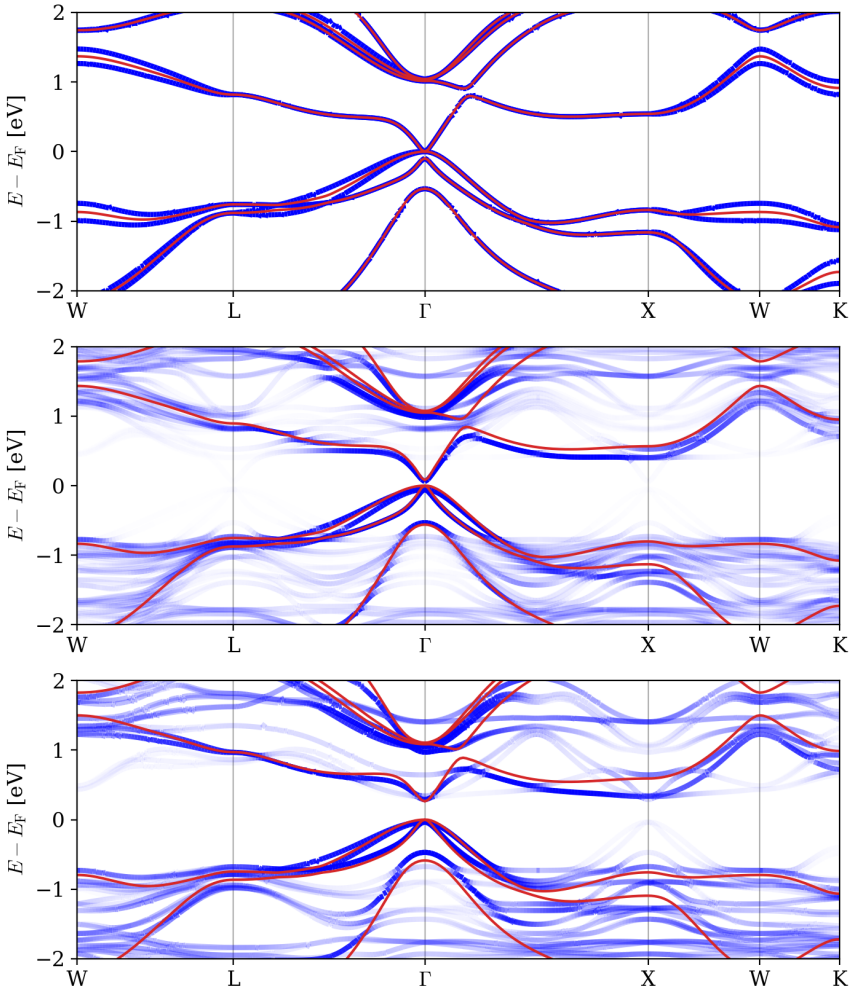

Figure 4.9: Unfolded band structure of supercells (blue) and VBA (red). The top pane shows the band structures of $La_8Pt_8Sb_8$ and the band structure of the relaxed LaPtSb primitive cell. The middle pane shows the band structures of $(LaPt)_7(ScNi)_1Sb_8$ and LaPtSb primitive cell with lattice constant reduced by 1%. The bottom pane shows the band structures of $(LaPt)_6(ScNi)_2Sb_8$ and LaPtSb primitive cell with lattice constant reduced by 2%.

Chapter 5

Discussion

This chapter will discuss the results presented in the previous chapter. For the high-throughput (HT) method, the methodology in itself will be discussed before attention is brought to the results. For volumetric band alignment (VBA) and the supercell calculations, most of the focus will be on the results. Finally, some thought will be given on what makes a good thermoelectric (TE) material in a more general sense.

5.1 High-throughput method

Through the use of PYTHON and Atomic Simulation Environment (ASE), scripts were developed that set up and submitted all the first principle calculations in this study, with the exception of the initial testing and supercell calculations. This worked well for this study and a similar method could with some improvements be implemented for much larger sets of materials.

Since this study only covered half-Heusler materials whose structures were provided by a colleague, the task of providing VASP crystal structure information did not require much consideration. For a larger study, however, this process might require some refinement, but as long as the crystal structure of materials is provided in a consistent format the task should be relatively simple.

Another problem for a larger study would be the analysis of data. For 67 materials the band structure and figure of merit (ZT) could be inspected by hand in a short period of time. For thousands of materials, this method would not be viable and some automatic measure of how likely the TE properties are to improve under volumetric changes would have to be implemented. Since some materials show great improvement to ZT under VBA despite at first appearing to be very poor TE materials this step

might be challenging. It would be possible to perform one or two calculations with different volumes and chose materials based on the increases in ZT, but this would double or triple the computational cost of the initial HT survey.

Lastly, there was not implemented any automatic verification that each calculation had completed correctly. While this was not a problem that was encountered during this study, a few calculations inevitably run into errors or crashes. An automatic procedure to check the results of all calculations and resubmit any that did not finish correctly should be fairly straightforward to implement.

5.2 Result from HT method

The full results for the HT-style calculations can be seen in Appendix A and Figure 4.1, 4.2 and 4.3. The ZT is plotted with respect to the Fermi energy for 2 eV in each direction from the top of the valence band. It is not necessarily possible to dope the Fermi energy that far, so ZT-peaks far from the band gap, such as for BaBiK, will generally be disregarded. The result will not in its entirety be compared to the calculated values of earlier work, but a selection of materials are shown in Figure 5.1 together with results from *Thermoelectric transport trends in group 4 half-Heusler alloys*[13]. The earlier work accounts for various phonon scattering mechanisms resulting in lower lattice thermal conductivity (κ_ℓ). To compare the electron transport properties calculated in this work on an even basis the values of ZT in this figure are calculated with the lattice thermal conductivity provided by the previous work, these are listed in Table D.1. The results seem to correlate well for most of the materials, though there are some exceptions.

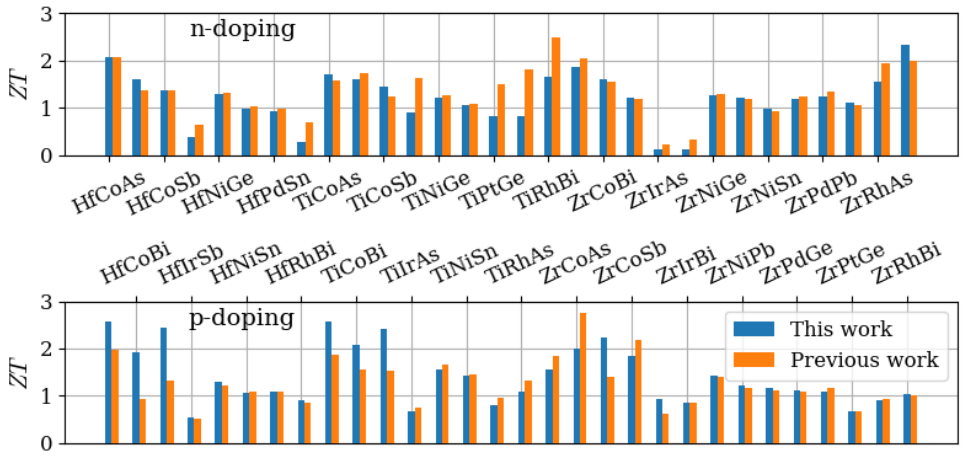

Figure 5.1: Comparison of ZT of this work and previous work[13] for a selection of materials. The values of ZT calculated with the lattice thermal conductivity provided by the previous work.

The three pairs of materials HfCoBi-HfCoSb, NbCoGe-NbIrSn, and ZrRhAs-ZrRhBi, see Section 4.1, were chosen for VBA for two reasons, along with having pretty good values for ZT. Firstly, they have band valleys that are close in energy level, for the HfCoBi-HfCoSb and NbCoGe-NbIrSn pairs, this is in the valence band, for ZrRhAs-ZrRhBi it is in the conduction band. Secondly, each pair are HH materials from the same group, meaning their three atoms have the same number of valence electrons. As shown in the results, each pair have strikingly similar band structures in the conduction and the valence band. Their similarity is a promising result for the VBA approximation which relies on this very fact. By choosing some pairs of materials like this there is also guaranteed to be some similar material to alloy with should the results from VBA show great improvement.

Another three materials, BiPdSc, LiZnSb, and TaRhAs, were chosen based on their band structure valleys. BiPdSc has two valleys in the conduction band that are very close in energy level which should require small volumetric changes to align, but still leaves some room for optimization. LiZnSb has larger energy differences in the conduction band valleys, but has the potential to align valleys on three high symmetry points should the conduction band change in the right way under volumetric changes. TaRhAs has three valence band valleys that are very close in energy and could potentially align four out of the five high symmetry points shown in the band structure.

LaRhTe only has two valleys in the conduction band, what is interesting is that one of these is between the high symmetry points Γ and X. Since the valley is fully within the first Brillouin zone and not on its boundary this valley will have twice the

degeneracy of the X-point resulting in a sharp rise in DOS close to the band gap. This results in LaRhTe having the highest Seebeck coefficient at maximum ZT among the relaxed materials, see Appendix C. The power factor is still rather low as electrical conductivity (σ) at maximum ZT is among the lowest of all the materials. A Fermi energy that results in a low σ also gives a low electron thermal conductivity (κ_e), as is shown in Figure 4.4. Since LaRhTe has such a low κ_ℓ having a low κ_e to maximize ZT. This also explains why the Fermi energy that maximizes PF does generally not result in the highest ZT.

Lastly, there is LaPtSb which has next to no band gap and the only band valley at each side is at the Γ-point making it seem unlikely to achieve any band alignment. This material was in fact first ignored, but some VBA calculations showed that valleys at the Γ-point generally seem to change more than those at other high symmetry points, see Figure 4.5 and Appendix B. Since LaPtSb also had a very low lattice thermal conductivity it was added to the materials chosen for VBA.

5.3 Volumetric band alignment

The VBA part of the study was implemented in a similar high-throughput way as the step before, but with a few adjustments to vary the lattice constant of the crystal structure. The results for four materials are shown in Section 4.3, the rest are shown in Appendix B.

LaRhTe is an example of a material that already has well aligned valleys in the conduction band and volume adjustments in either direction cause a reduction in ZT. This not surprising as the well aligned conduction band with a valley between high symmetry points along with a very low lattice thermal conductivity gives the relaxed structure a high ZT initially. No literature has been found that confirms or rejects this value, though there are several that has predicted a low lattice thermal conductivity[47][52], usually reported as RhLaTe. Another interesting observation is how the figure of merit changes with the different valleys. When the Γ-point becomes dominant ZT quickly drops to about 20%, but when the opposite happens ZT still remains at about 90%. This illustrates the importance of the degeneracy of the band valleys and how it changes the effective mass[53].

LiZnSb and TaRhSn both show great examples of band aligning when the volume is changed. While LiZnSb already had two valleys aligned a reduction in volume causes the L-point to align with the X-point rather than the Γ-point. Again, the increased degeneracy results in ZT nearly doubling. Arguably, the results from more calculations with further reduction in volume would have been appropriate here, but from the changes in the band structure, it seems likely that further reduction of volume would increase the energy level of the L-point until it would no longer be aligned with the X-point. TaRhSn amazingly shows alignment of valleys at four out of five high symmetry points. ZT does not increase as much in this case, but compared to LiZnSb, TaRhSn has a much higher lattice thermal conductivity. This conductivity would likely decrease in an alloy[13][54] and could possibly increasing ZT significantly.

VBA of LaPtSb showed that reducing the volume increased ZT as the energy level of the Γ-point increased, making the valley between the Γ-point and the X-point contribute. At its highest, ZT reached 3.5, an increase of more than 100% and the highest calculated ZT in this study. Since LaPtSb shows both a significant change in ZT and band structure the decision was made to try to replicate these changes by supercell calculations with ScNiSb. This is not one of the materials that have been part of earlier calculations and has by some studies been predicted to be unstable[47].

The remaining materials showed varying results under VBA. Some materials showed improvements, but most only by a small margin, see Appendix B. An interesting "side-effect" of VBA is that changing the volume can increase the band gap, an example of this is shown in Figure 4.8. This could help find good TE materials that have previously been discarded for having little to no band gap. Predicting a lower

than real band gap is a common problem within density functional theory[32]. A more thorough survey should still employ more exchange-correlation functionals that perform better in this regard, such as PBEsol[55].

5.4 Supercell verification

Figure 4.9 shows how the unfolded band structures of $(LaPt)_{8-x}(ScNi)_xSb_8$ changes in supercell with x= $0, 1, 2$. In each plot, a band structure from VBA is also included. The unfolding software[45] reconstructs the band structure nicely for a pure LaPtSb supercell, but when ScNiSb is mixed in much of the band structure becomes difficult to recreate. It is possible that the choice of alloying with ScNiSb was too aggressive since it changes two of the elements in the structure making the band structure too different. The reason for this choice was that the lattice constant is smaller than for materials where only one atom is changed, making a large enough reduction in the supercell volume possible with only one or two substitutions. The poor band structures can also be an indication that the materials are not soluble. For materials that are more similar, the same software has been shown to produce much better reconstructions of the primitive cell band structure. This is demonstrated in Figure 5.2 with the unfolded band structure of two $2\times2\times2$ supercells containing $Zr_8Ni_8Sn_8$ and $Zr_8Ni_8Sn_7Pb_1$. There are a lot fewer disturbances to the band structure between the pure supercell and the alloy. The LDOS presented in Figure 4.2 shows that Sb contributes less to the total DOS in the area suggesting it would cause less disturbance to the band structure in an alloy. Unfortunately, the lattice constant of LaPtAs is only about 2.6% lower than LaPtSb making the necessary volume changes impossible.

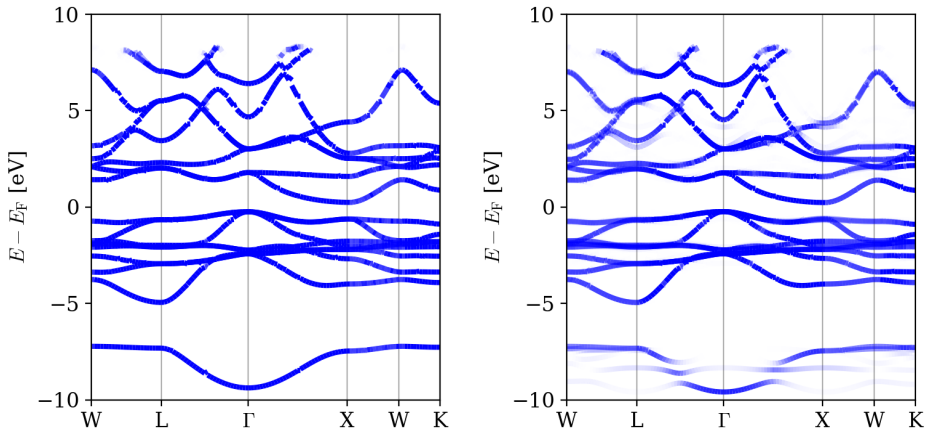

Figure 5.2: Unfolded band structure of $Zr_8Ni_8Sn_8$ and $Zr_8Ni_8Sn_7Pb_1$

Luckily, the conduction and the valance band in the area around the Γ-point are quite clear and can be compared to the band structure from VBA. The energy levels of the conduction and valance band change in the same way in the supercell calculation and VBA. This is a promising result and indicates that there is some merit to the VBA approximation, however, a solid conclusion should probably not be drawn from this result alone. The electronic transport properties of the supercell

were not calculated with BoltzTraP2. The reason for this is that the constant relaxation time approximation is unlikely to hold up well in a periodic structure disturbed by alloying, as the supercells create false periodicity and do not introduce explicit scattering mechanisms, according to K. Berland.

The inconclusive results from the supercell calculations means that the validity of the VBA approximation based on this study is still uncertain. While Bhattacharya and Madsen do a thorough verification process they also suggest that "systems allowing VBA are quite rare"[22] so applying it to any material might be too optimistic. Before any large-scale survey is performed the conditions under which this approximation holds should be tested rigorously. In this study the lattice constant has been changed by up to 5%, this could be way beyond what can be accurately approximated by VBA.

5.5 General considerations

This study has calculated the thermoelectric properties of 67 HH materials in an attempt to find better TE materials. However, the materials have only been considered in terms of the thermoelectric figure of merit. There are a lot more factors that should be considered in a more detailed work.

While all the 67 materials have been predicted to be stable by first principle calculations in one previous study[47] there are other studies that disagree for some materials[56]. It is also unlikely that all the materials are stable under the volume changes imposed by VBA. Nor is there any guarantee the there even exists any stable material to alloy with that allows for volume change in the desired direction.

Many of the materials in this study also have other properties that would make them less desirable. Arsenic, lead, cobalt, and several other elements can be toxic. Gold and platinum are very expensive, along with many other elements included here. For some niche applications, such as deep space probes this might not be a problem, but if any thermoelectric material is going to help tackle the global use of fossil fuels, factors like price, availability, environmental impact, and health issues would have to be considered carefully.

Chapter 6

Conclusion and further work

6.1 Conclusion

In this study, an early method for performing a high-throughput survey of thermoelectric materials based on first principle calculations has been developed. A subset of materials was then investigated further by approximating alloying with volumetric band alignment. Then, verification of the results from the volumetric band alignment was attempted through supecell calculations.

The high-throughput method was found to work well for the number of materials selected for this study. Still, some improvements would have to be made before it could be implemented for a true high-throughput study. Some materials were compared to previous first principle studies and the results correlate well. LaRhTe was predicted to has a figure of merit of 2.7, a material that have yet to be seen in literature in the context of thermoelectricity. Several other materials showed interesting features in the band structure.

The results from volumetric band alignment show that the predicted band structure can change a lot based on the volume. Some materials were found to be close to the best possible alignment of band valleys and volumetric changes only reduced the thermoelectric properties. Others showed great improvement in the figure of merit as band valleys aligned, most notably LaPtSb with a predicted figure of merit of 3.5. If volumetric band alignment generally is an accurate approximation of alloying, this method could find optimized alloys in a much less computationally expensive way than most other methods currently in use. The supercell calculations somewhat suggest that parts of the band structure change in the same way under alloying and volumetric band alignment for some materials.

6.2 Further work

There is much work that could expand on this study. Future work can be roughly grouped into four different categories. Firstly, expand the number of materials searched to a true high throughput survey, and try to optimize them with volumetric band alignment. There are thousands of materials that could potentially be good thermoelectric (TE) materials. Many might have been discarded because the relaxed structures show poor TE properties, many might have never been investigated at all. With a computationally inexpensive way to approximate alloys the space of materials that is viable to search expands greatly.

Secondly, increase the accuracy of the first principle and thermoelectric property calculations. By using exchange-correlation functionals such as PBEsol[55] or hybrid functionals[57] the band structure of different materials can be calculated more precisely. This could avoid inaccuracies such as predicting too low band gaps, a well-known problem within density functional theory[32]. The calculation of the TE properties can also be refined. By abandoning the constant relaxation time approximation, an already existing possibility within BoltzTraP2, the electron transport properties can be calculated in a more precise manner[31]. Similarly, the calculation of the lattice thermal conductivity could be expanded to include more scattering mechanisms which is likely to produce a lower thermal conductivity[13].

Thirdly, expand the size of the first principle calculations. By performing supercell calculations, larger than was had been done in this study, the properties of alloys can be described more accurately. This could help verify or dismiss the correctness of the approximations of volumetric band alignment. By including techniques such as special quasirandom structures[58] leading to a widening of the band structure[59] the disorder of a bulk material can be more accurately predicted.

Lastly, combine computations with experimental results. When more accurate calculations have, with high probability, predicted a material with good TE properties, it could be synthesized and tested. This would be the final step in confirming the properties of a bulk TE material and could evaluate the accuracy of the first principle calculations.

Bibliography

[1] H. Ritchie and M. Roser, "Energy," *Our World in Data*, 2020, https://ourworldindata.org/energy.

[2] IPCC, *Climate Change 2013: The Physical Science Basis. Contribution of Working Group I to the Fifth Assessment Report of the Intergovernmental Panel on Climate Change*. Cambridge, United Kingdom and New York, NY, USA: Cambridge University Press, 2013. [Online]. Available: www.climatechange2013.org

[3] J. M. Cullen and J. M. Allwood, "Theoretical efficiency limits for energy conversion devices," *Energy*, vol. 35, no. 5, pp. 2059–2069, 2010. [Online]. Available: https://www.sciencedirect.com/science/article/pii/S0360544210000265

[4] C. Forman, I. K. Muritala, R. Pardemann, and B. Meyer, "Estimating the global waste heat potential," *Renewable and Sustainable Energy Reviews*, vol. 57, pp. 1568–1579, 2016. [Online]. Available: https://www.sciencedirect.com/science/article/pii/S1364032115015750

[5] A. D. LaLonde, Y. Pei, H. Wang, and G. Jeffrey Snyder, "Lead telluride alloy thermoelectrics," *Materials Today*, vol. 14, no. 11, pp. 526–532, 2011. [Online]. Available: https://www.sciencedirect.com/science/article/pii/S1369702111702784

[6] Y. Ding, Y. Qiu, K. Cai, Q. Yao, S. Chen, L. Chen, and J. He, "High performance n-type ag2se film on nylon membrane for flexible thermoelectric power generator," *Nature Communications*, vol. 10, no. 1, p. 841, Feb 2019. [Online]. Available: https://doi.org/10.1038/s41467-019-08835-5

[7] K. Bartholomé, B. Balke, D. Zuckermann, M. Köhne, M. Müller, K. Tarantik, and J. König, "Thermoelectric modules based on half-heusler materials produced in large quantities," *Journal of Electronic Materials*, vol. 43, no. 6, pp. 1775–1781, Jun 2014. [Online]. Available: https://doi.org/10.1007/s11664-013-2863-x

[8] R. Moshwan, L. Yang, J. Zou, and Z.-G. Chen, "Eco-friendly snte thermoelectric materials: Progress and future challenges," *Advanced Functional Materials*, vol. 27, no. 43, p. 1703278, 2017. [Online]. Available: https://onlinelibrary.wiley.com/doi/abs/10.1002/adfm.201703278

[9] K. Biswas, J. He, I. D. Blum, C.-I. Wu, T. P. Hogan, D. N. Seidman, V. P. Dravid, and M. G. Kanatzidis, "High-performance bulk thermoelectrics with all-scale hierarchical architectures," *Nature*, vol. 489, no. 7416, pp. 414–418, Sep 2012. [Online]. Available: https://doi.org/10.1038/nature11439

[10] G. J. Snyder and E. S. Toberer, "Complex thermoelectric materials," *Nature Materials*, vol. 7, no. 2, pp. 105–114, Feb 2008. [Online]. Available: https://doi.org/10.1038/nmat2090

[11] G. Chen, M. S. Dresselhaus, G. Dresselhaus, J.-P. Fleurial, and T. Caillat, "Recent developments in thermoelectric materials," *International Materials Reviews*, vol. 48, no. 1, pp. 45–66, 2003. [Online]. Available: https://doi.org/10.1179/095066003225010182

[12] O. Løvvik, E. Flage-Larsen, and G. Skomedal, "Screening of thermoelectric silicides with atomistic transport calculations," *Journal of Applied Physics*, vol. 128, p. 125105, 09 2020. [Online]. Available: https://www.researchgate.net/publication/345416049_Screening_of_thermoelectric_silicides_with_atomistic_transport_calculations

[13] K. Berland, N. Shulumba, O. Hellman, C. Persson, and O. Løvvik, "Thermoelectric transport trends in group 4 half-heusler alloys," 07 2019. [Online]. Available: https://www.researchgate.net/publication/334288763_Thermoelectric_transport_trends_in_group_4_half-Heusler_alloys

[14] H. Zhu, G. Hautier, U. Aydemir, Z. M. Gibbs, G. Li, S. Bajaj, J.-H. Pöhls, D. Broberg, W. Chen, A. Jain, M. A. White, M. Asta, G. J. Snyder, K. Persson, and G. Ceder, "Computational and experimental investigation of tmagte2 and xyz2 compounds, a new group of thermoelectric materials identified by first-principles high-throughput screening," *J. Mater. Chem. C*, vol. 3, pp. 10 554–10 565, 2015. [Online]. Available: http://dx.doi.org/10.1039/C5TC01440A

[15] C. B. Satterthwaite and R. W. Ure, "Electrical and thermal properties of bi_2 te_3," *Phys. Rev.*, vol. 108, pp. 1164–1170, Dec 1957. [Online]. Available: https://link.aps.org/doi/10.1103/PhysRev.108.1164

[16] Y. Pei, H. Wang, and G. J. Snyder, "Band engineering of thermoelectric materials," *Advanced Materials*, vol. 24, no. 46, pp. 6125–6135, 2012. [Online]. Available: https://onlinelibrary.wiley.com/doi/abs/10.1002/adma.201202919

[17] J. P. Dismukes, L. Ekstrom, E. F. Steigmeier, I. Kudman, and D. S. Beers, "Thermal and electrical properties of heavily doped ge-si alloys up to 1300°k," *Journal of Applied Physics*, vol. 35, no. 10, pp. 2899–2907, 1964. [Online]. Available: https://doi.org/10.1063/1.1713126

[18] H. Xie, H. Wang, C. Fu, Y. Liu, G. J. Snyder, X. Zhao, and T. Zhu, "The intrinsic disorder related alloy scattering in zrnisn half-heusler thermoelectric materials," *Scientific Reports*, vol. 4, no. 1, p. 6888, Nov 2014. [Online]. Available: https://doi.org/10.1038/srep06888

[19] S. S. Shastri and S. K. Pandey, "Thermoelectric properties, efficiency and thermal expansion of ZrNiSn half-heusler by first-principles calculations," *Journal of Physics: Condensed Matter*, vol. 32, no. 35, p. 355705, jun 2020. [Online]. Available: https://doi.org/10.1088/1361-648x/ab8b9e

[20] Y. Liu, C. Fu, K. Xia, J. Yu, X. Zhao, H. Pan, C. Felser, and T. Zhu, "Lanthanide contraction as a design factor for high-performance half-heusler thermoelectric materials," *Advanced Materials*, vol. 30, no. 32, p. 1800881, 2018. [Online]. Available: https://onlinelibrary.wiley.com/doi/abs/10.1002/adma.201800881

[21] P. Pichanusakorn and P. Bandaru, "Nanostructured thermoelectrics," *Materials Science and Engineering: R: Reports*, vol. 67, no. 2, pp. 19–63, 2010. [Online]. Available: https://www.sciencedirect.com/science/article/pii/S0927796X09000904

[22] S. Bhattacharya and G. K. H. Madsen, "High-throughput exploration of alloying as design strategy for thermoelectrics," *Phys. Rev. B*, vol. 92, p. 085205, Aug 2015. [Online]. Available: https://link.aps.org/doi/10.1103/PhysRevB.92.085205

[23] J. He and T. Tritt, "Advances in thermoelectric materials research: Looking back and moving forward," *Science*, vol. 357, p. eaak9997, 09 2017.

[24] C. Goupil, *Continuum Theory and Modeling of Thermoelectric Elements*, 01 2016.

[25] N. W. Ashcroft and N. D. Mermin, *Solid State Physics*. Holt-Saunders, 1976.

[26] M. Lundstrom, *Fundamentals of Carrier Transport*, 2nd ed. Cambridge University Press, 2000.

[27] G. Kumar, G. Prasad, and R. Pohl, "Experimental determinations of the lorenz number," *Journal of Materials Science*, vol. 28, pp. 4261–4272, 01 1993.

[28] F. Casper, T. Graf, S. Chadov, B. Balke, and C. Felser, "Half-heusler compounds: novel materials for energy and spintronic applications," *Semiconductor Science and Technology*, vol. 27, no. 6, p. 063001, apr 2012. [Online]. Available: https://doi.org/10.1088/0268-1242/27/6/063001

[29] D. Xiao, Y. Yao, W. Feng, J. Wen, W. Zhu, X.-Q. Chen, G. M. Stocks, and Z. Zhang, "Half-heusler compounds as a new class of three-dimensional topological insulators," *Phys. Rev. Lett.*, vol. 105, p. 096404, Aug 2010. [Online]. Available: https://link.aps.org/doi/10.1103/PhysRevLett.105.096404

[30] T. Zhu, C. Fu, H. Xie, Y. Liu, and X. Zhao, "High efficiency half-heusler thermoelectric materials for energy harvesting," *Advanced Energy Materials*, vol. 5, no. 19, p. 1500588, 2015. [Online]. Available: https://onlinelibrary.wiley.com/doi/abs/10.1002/aenm.201500588

[31] G. K. Madsen, J. Carrete, and M. J. Verstraete, "Boltztrap2, a program for interpolating band structures and calculating semi-classical transport

coefficients," *Computer Physics Communications*, vol. 231, pp. 140–145, 2018. [Online]. Available: https://www.sciencedirect.com/science/article/pii/S0010465518301632

[32] C. Persson and K. Berland, "Brief introduction to the density functional theory," 2016.

[33] D. J. Griffiths, *Introduction to Quantum Mechanics (2nd Edition)*, 2nd ed. Pearson Prentice Hall, Apr. 2004. [Online]. Available: http://www.amazon.com/exec/obidos/redirect?tag=citeulike07-20&path=ASIN/0131118927

[34] D. R. Hartree, "The wave mechanics of an atom with a non-coulomb central field. part ii. some results and discussion," *Mathematical Proceedings of the Cambridge Philosophical Society*, vol. 24, no. 1, p. 111–132, 1928.

[35] D. R. Hartree and W. Hartree, "Self-consistent field, with exchange, for beryllium," *Proceedings of the Royal Society of London. Series A - Mathematical and Physical Sciences*, vol. 150, no. 869, pp. 9–33, 1935. [Online]. Available: https://royalsocietypublishing.org/doi/abs/10.1098/rspa.1935.0085

[36] P. Hohenberg and W. Kohn, "Inhomogeneous electron gas," *Phys. Rev.*, vol. 136, pp. B864–B871, Nov 1964. [Online]. Available: https://link.aps.org/doi/10.1103/PhysRev.136.B864

[37] W. Kohn and L. J. Sham, "Self-consistent equations including exchange and correlation effects," *Phys. Rev.*, vol. 140, pp. A1133–A1138, Nov 1965. [Online]. Available: https://link.aps.org/doi/10.1103/PhysRev.140.A1133

[38] F. Bloch, "Über die Quantenmechanik der Elektronen in Kristallgittern," *Zeitschrift fur Physik*, vol. 52, no. 7-8, pp. 555–600, Jul. 1929.

[39] J. P. Perdew and Y. Wang, "Accurate and simple analytic representation of the electron-gas correlation energy," *Phys. Rev. B*, vol. 45, pp. 13 244–13 249, Jun 1992. [Online]. Available: https://link.aps.org/doi/10.1103/PhysRevB.45.13244

[40] J. P. Perdew, K. Burke, and M. Ernzerhof, "Generalized gradient approximation made simple," *Phys. Rev. Lett.*, vol. 77, pp. 3865–3868, Oct 1996. [Online]. Available: https://link.aps.org/doi/10.1103/PhysRevLett.77.3865

[41] G. Kresse and J. Hafner, "Ab initio molecular dynamics for liquid metals," *Phys. Rev. B*, vol. 47, pp. 558–561, Jan 1993. [Online]. Available: https://link.aps.org/doi/10.1103/PhysRevB.47.558

[42] P. E. Blöchl, "Projector augmented-wave method," *Phys. Rev. B*, vol. 50, pp. 17 953–17 979, Dec 1994. [Online]. Available: https://link.aps.org/doi/10.1103/PhysRevB.50.17953

[43] A. H. Larsen, J. J. Mortensen, J. Blomqvist, I. E. Castelli, R. Christensen, M. Dułak, J. Friis, M. N. Groves, B. Hammer, C. Hargus, E. D. Hermes, P. C. Jennings, P. B. Jensen, J. Kermode, J. R. Kitchin, E. L. Kolsbjerg, J. Kubal, K. Kaasbjerg, S. Lysgaard, J. B. Maronsson, T. Maxson, T. Olsen, L. Pastewka,

A. Peterson, C. Rostgaard, J. Schiøtz, O. Schütt, M. Strange, K. S. Thygesen, T. Vegge, L. Vilhelmsen, M. Walter, Z. Zeng, and K. W. Jacobsen, "The atomic simulation environment—a python library for working with atoms," *Journal of Physics: Condensed Matter*, vol. 29, no. 27, p. 273002, jun 2017. [Online]. Available: https://doi.org/10.1088/1361-648x/aa680e

[44] M. A. Jette, A. B. Yoo, and M. Grondona, "Slurm: Simple linux utility for resource management," in *In Lecture Notes in Computer Science: Proceedings of Job Scheduling Strategies for Parallel Processing (JSSPP) 2003*. Springer-Verlag, 2002, pp. 44–60.

[45] U. Herath, P. Tavadze, X. He, E. Bousquet, S. Singh, F. Muñoz, and A. H. Romero, "Pyprocar: A python library for electronic structure pre/post-processing," *Computer Physics Communications*, vol. 251, p. 107080, Jun 2020. [Online]. Available: http://dx.doi.org/10.1016/j.cpc.2019.107080

[46] S. P. Ong, W. D. Richards, A. Jain, G. Hautier, M. Kocher, S. Cholia, D. Gunter, V. L. Chevrier, K. A. Persson, and G. Ceder, "Python materials genomics (pymatgen): A robust, open-source python library for materials analysis," *Computational Materials Science*, vol. 68, pp. 314–319, 2013. [Online]. Available: https://www.sciencedirect.com/science/article/pii/S0927025612006295

[47] J. Carrete, W. Li, N. Mingo, S. Wang, and S. Curtarolo, "Finding unprecedentedly low-thermal-conductivity half-heusler semiconductors via high-throughput materials modeling," *Phys. Rev. X*, vol. 4, p. 011019, Feb 2014. [Online]. Available: https://link.aps.org/doi/10.1103/PhysRevX.4.011019

[48] P. Wisesa, K. A. McGill, and T. Mueller, "Efficient generation of generalized monkhorst-pack grids through the use of informatics," *Phys. Rev. B*, vol. 93, p. 155109, Apr 2016. [Online]. Available: https://link.aps.org/doi/10.1103/PhysRevB.93.155109

[49] G. P. Francis and M. C. Payne, "Finite basis set corrections to total energy pseudopotential calculations," *Journal of Physics: Condensed Matter*, vol. 2, no. 19, pp. 4395–4404, may 1990. [Online]. Available: https://doi.org/10.1088/0953-8984/2/19/007

[50] H. J. Monkhorst and J. D. Pack, "Special points for brillouin-zone integrations," *Phys. Rev. B*, vol. 13, pp. 5188–5192, Jun 1976. [Online]. Available: https://link.aps.org/doi/10.1103/PhysRevB.13.5188

[51] A. R. Denton and N. W. Ashcroft, "Vegard's law," *Phys. Rev. A*, vol. 43, pp. 3161–3164, Mar 1991. [Online]. Available: https://link.aps.org/doi/10.1103/PhysRevA.43.3161

[52] Z. Feng, Y. Fu, Y. Zhang, and D. J. Singh, "Characterization of rattling in relation to thermal conductivity: Ordered half-heusler semiconductors," *Physical Review B*, vol. 101, no. 6, 2 2020. [Online]. Available: https://www.osti.gov/biblio/1597047

[53] Y. Tang, Z. M. Gibbs, L. A. Agapito, G. Li, H.-S. Kim, M. Nardelli, S. Curtarolo, and G. J. Snyder, "Convergence of multi-valley bands as the electronic origin of high thermoelectric performance in cosb3 skutterudites," *Nature Materials*, vol. 14, no. 12, pp. 1223–1228, Dec 2015. [Online]. Available: https://doi.org/10.1038/nmat4430

[54] S. N. H. Eliassen, A. Katre, G. K. H. Madsen, C. Persson, O. M. Løvvik, and K. Berland, "Lattice thermal conductivity of $ti_xzr_yhf_{1-x-y}$NiSn half-heusler alloys calculated from first principles: Key role of nature of phonon modes," *Phys. Rev. B*, vol. 95, p. 045202, Jan 2017. [Online]. Available: https://link.aps.org/doi/10.1103/PhysRevB.95.045202

[55] J. P. Perdew, A. Ruzsinszky, G. I. Csonka, O. A. Vydrov, G. E. Scuseria, L. A. Constantin, X. Zhou, and K. Burke, "Restoring the density-gradient expansion for exchange in solids and surfaces," *Phys. Rev. Lett.*, vol. 100, p. 136406, Apr 2008. [Online]. Available: https://link.aps.org/doi/10.1103/PhysRevLett.100.136406

[56] R. Gautier, X. Zhang, L. Hu, L. Yu, Y. Lin, T. Sunde, D. Chon, K. Poeppelmeier, and A. Zunger, "Prediction and accelerated laboratory discovery of previously unknown 18-electron abx compounds," *Nature Chemistry*, vol. 7, no. 4, pp. 308–316, Apr. 2015, publisher Copyright: © 2015 Macmillan Publishers Limited.

[57] K. Berland and C. Persson, "Thermoelectric transport of gaas, inp, and pbte: Hybrid functional with $k \cdot p$ interpolation versus scissor-corrected generalized gradient approximation," *Journal of Applied Physics*, vol. 123, 03 2018.

[58] A. Zunger, S.-H. Wei, L. G. Ferreira, and J. E. Bernard, "Special quasirandom structures," *Phys. Rev. Lett.*, vol. 65, pp. 353–356, Jul 1990. [Online]. Available: https://link.aps.org/doi/10.1103/PhysRevLett.65.353

[59] V. Popescu and A. Zunger, "Extracting e versus k effective band structure from supercell calculations on alloys and impurities," *Phys. Rev. B*, vol. 85, p. 085201, Feb 2012. [Online]. Available: https://link.aps.org/doi/10.1103/PhysRevB.85.085201

Appendices

Appendix A

High-throughput result

Figure A.1-A.14 show the local density of states (LDOS), band structure and figure of merit (ZT) for the 56 materials that were not chosen for volumetric band alignment (VBA).

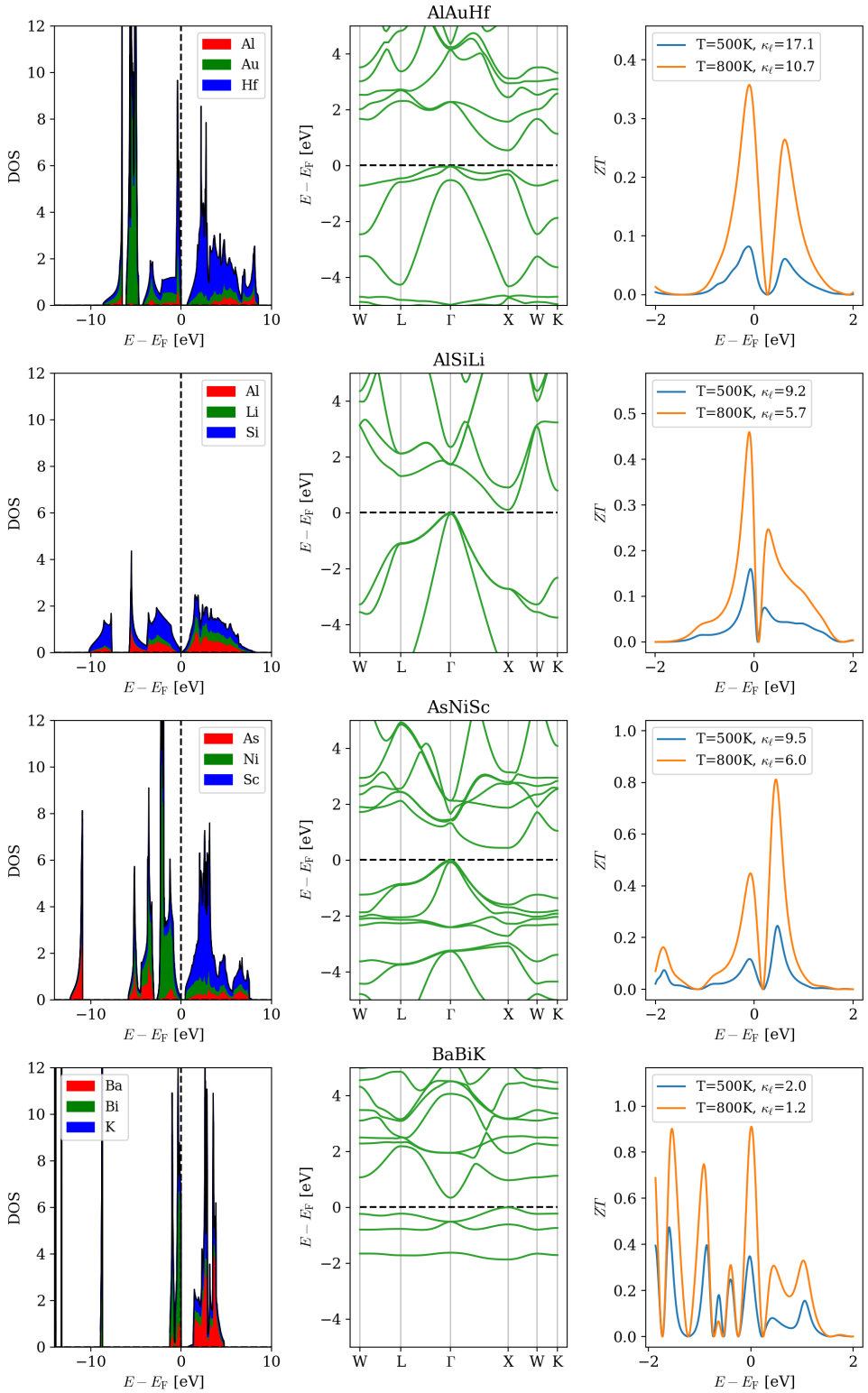

Figure A.1: LDOS, band structure, and ZT for AlAuHf, AlSiLi, AsNiSc and BaBiK.

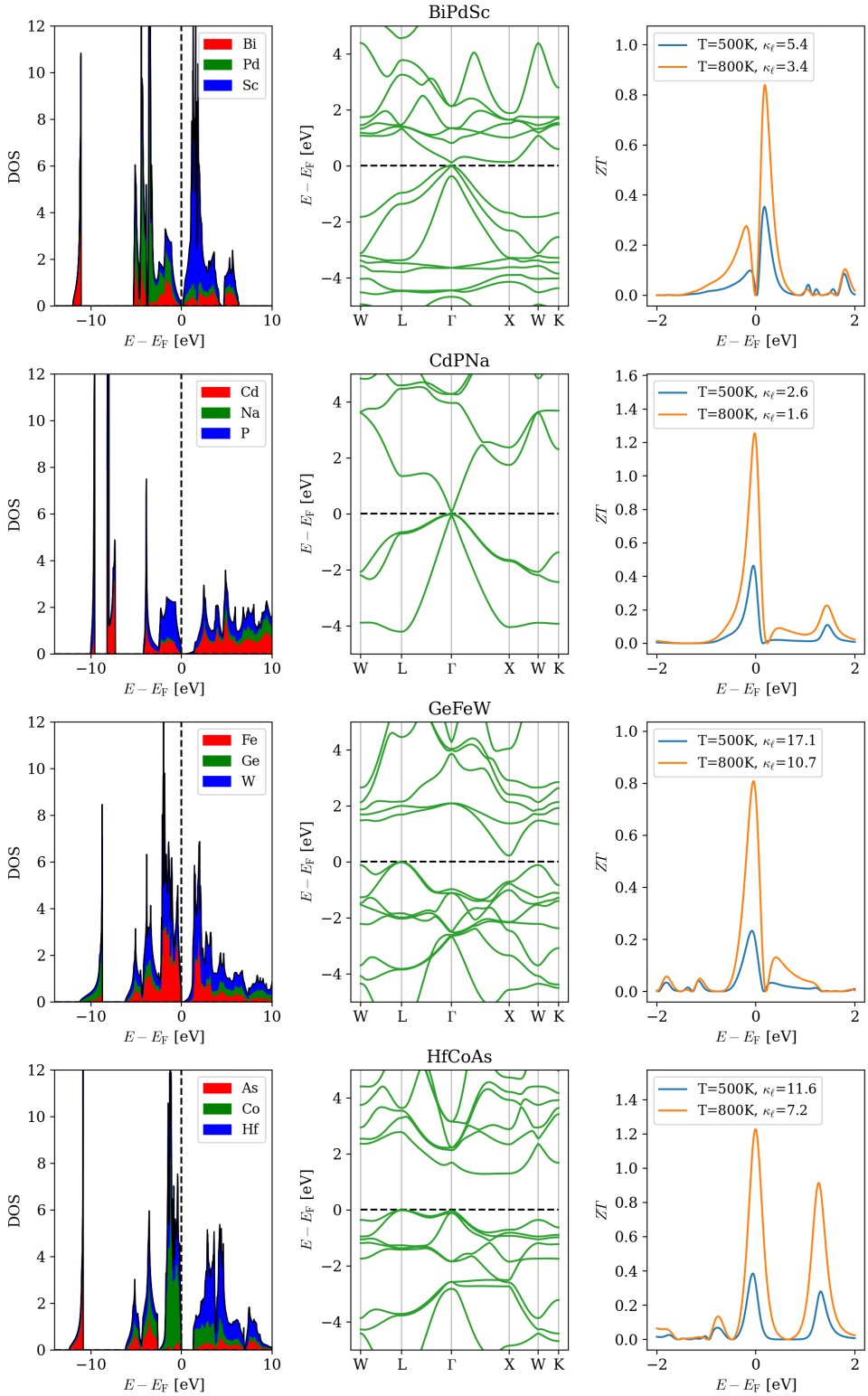

Figure A.2: LDOS, band structure and ZT for BiPdSc, CdPNa, GeFeW, and HfCoAs.

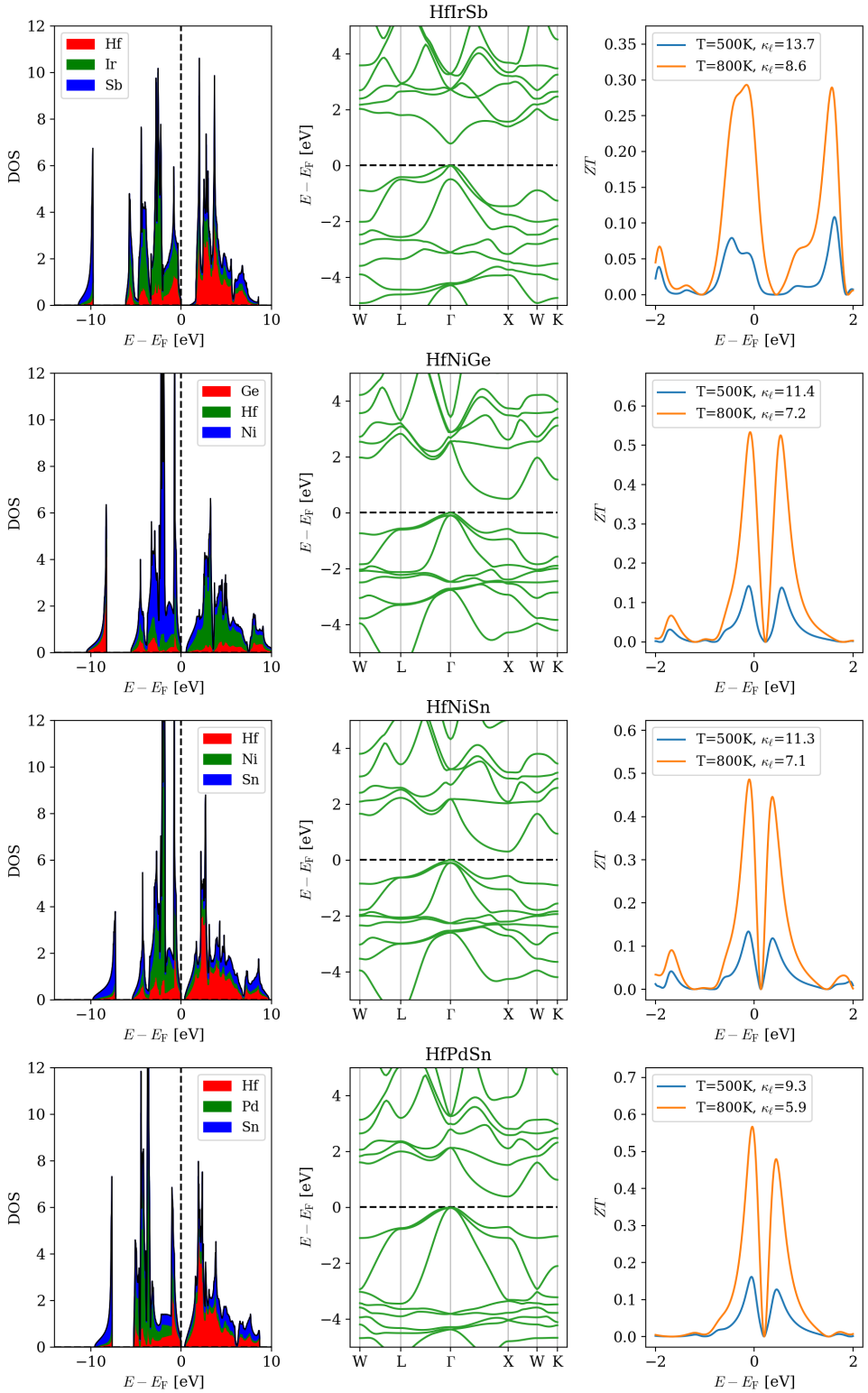

Figure A.3: LDOS, band structure and ZT for HfIrSb, HfNiGr, HfNiSn, and HfPdSn.

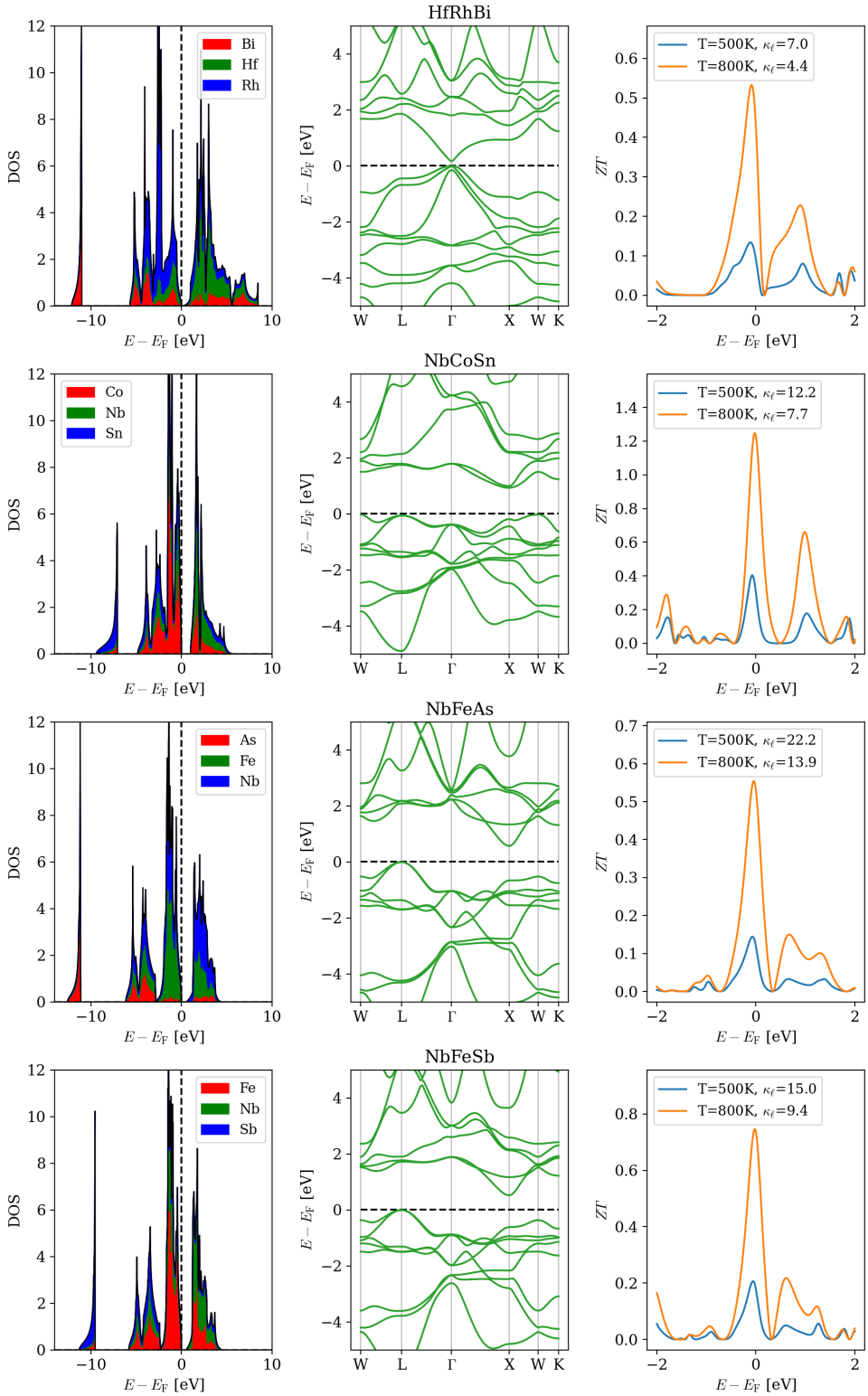

Figure A.4: LDOS, band structure and ZT for HfRhBi, NbCoSn, NbFeAs, and NbFeSb.

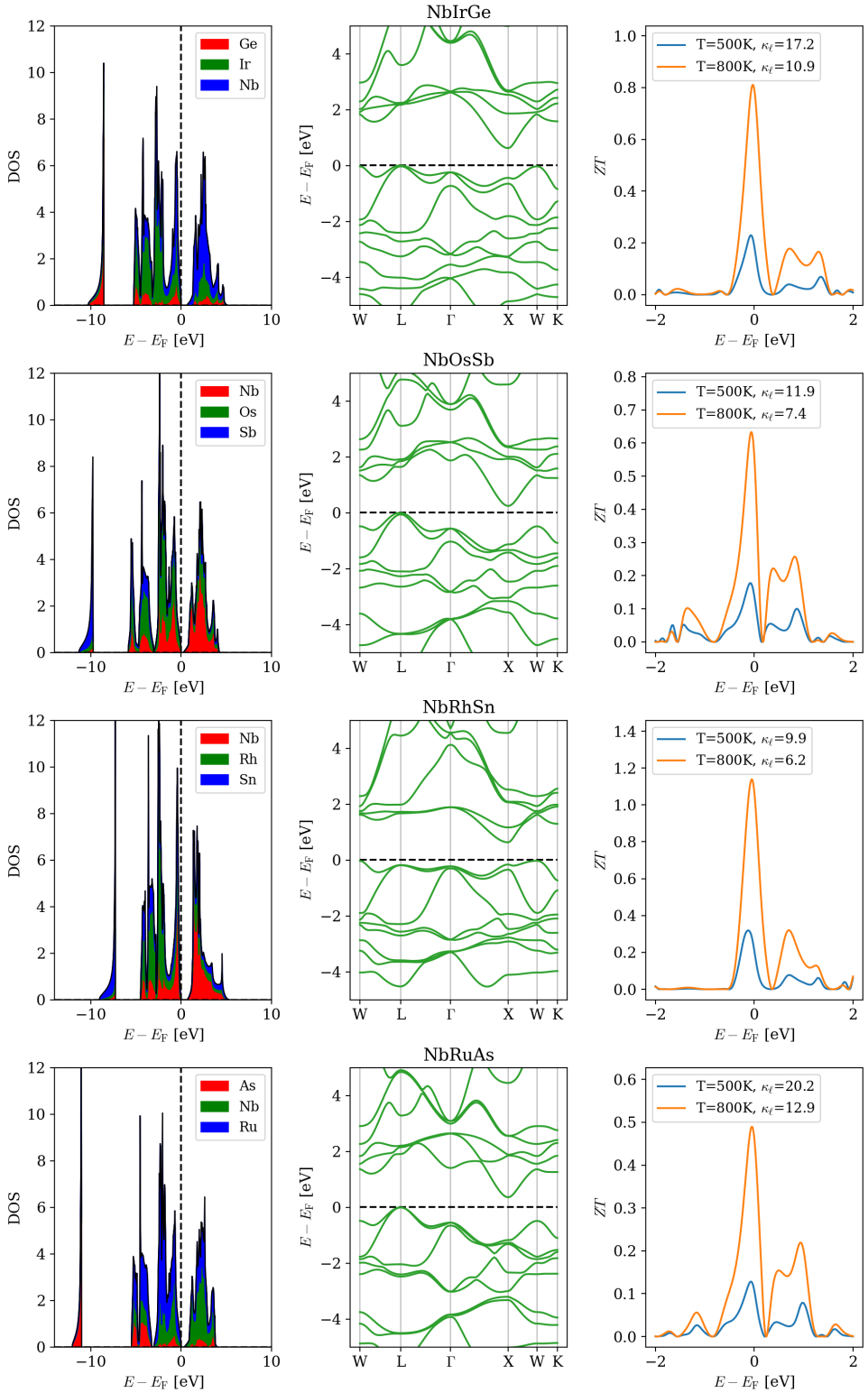

Figure A.5: LDOS, band structure and ZT for NbIrGe, NbOsSb, NbRhSn, and NbRuAs.

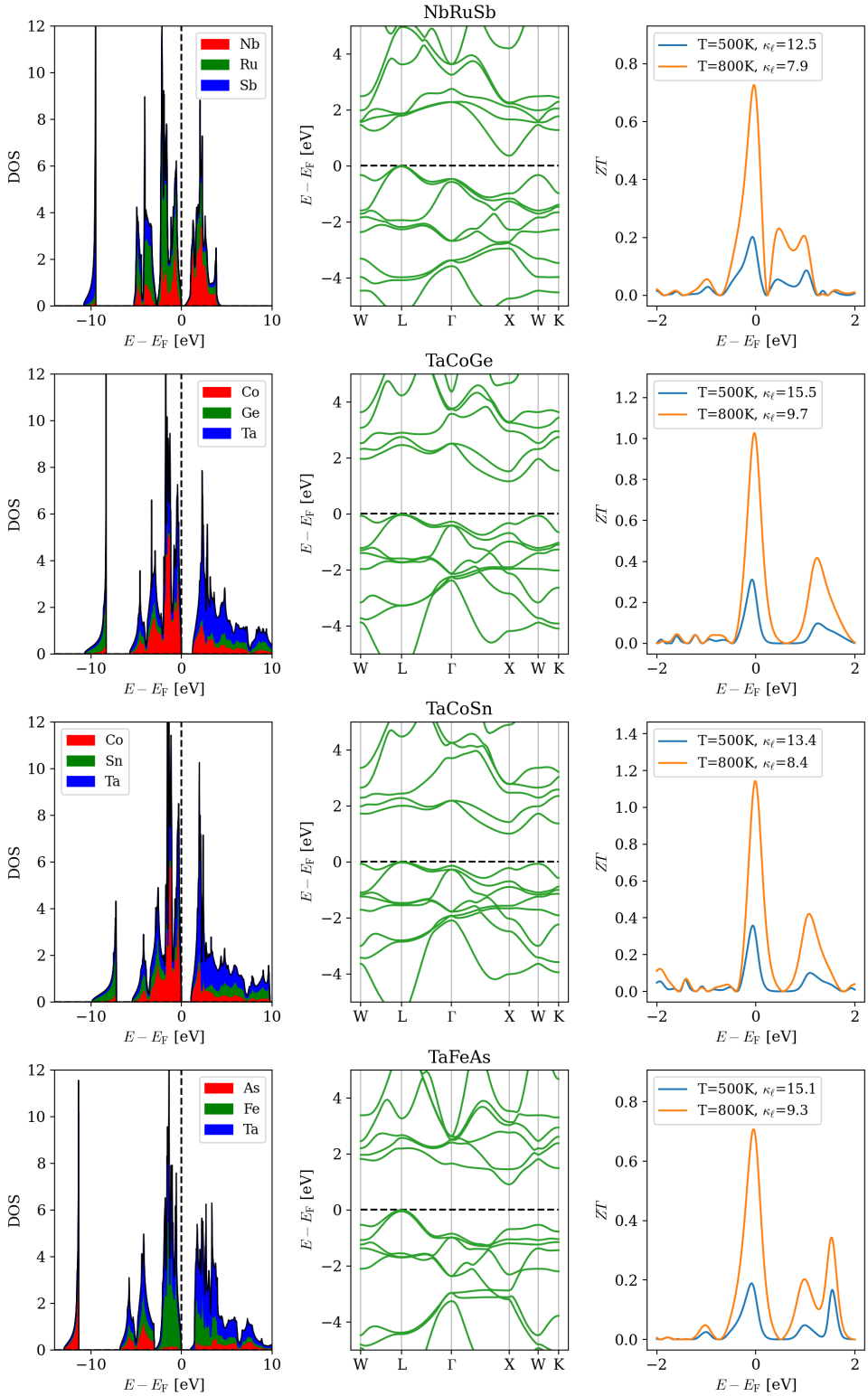

Figure A.6: LDOS, band structure and ZT for NbRuSb, TaCoGe, TaCoSn, and TaFeAs.

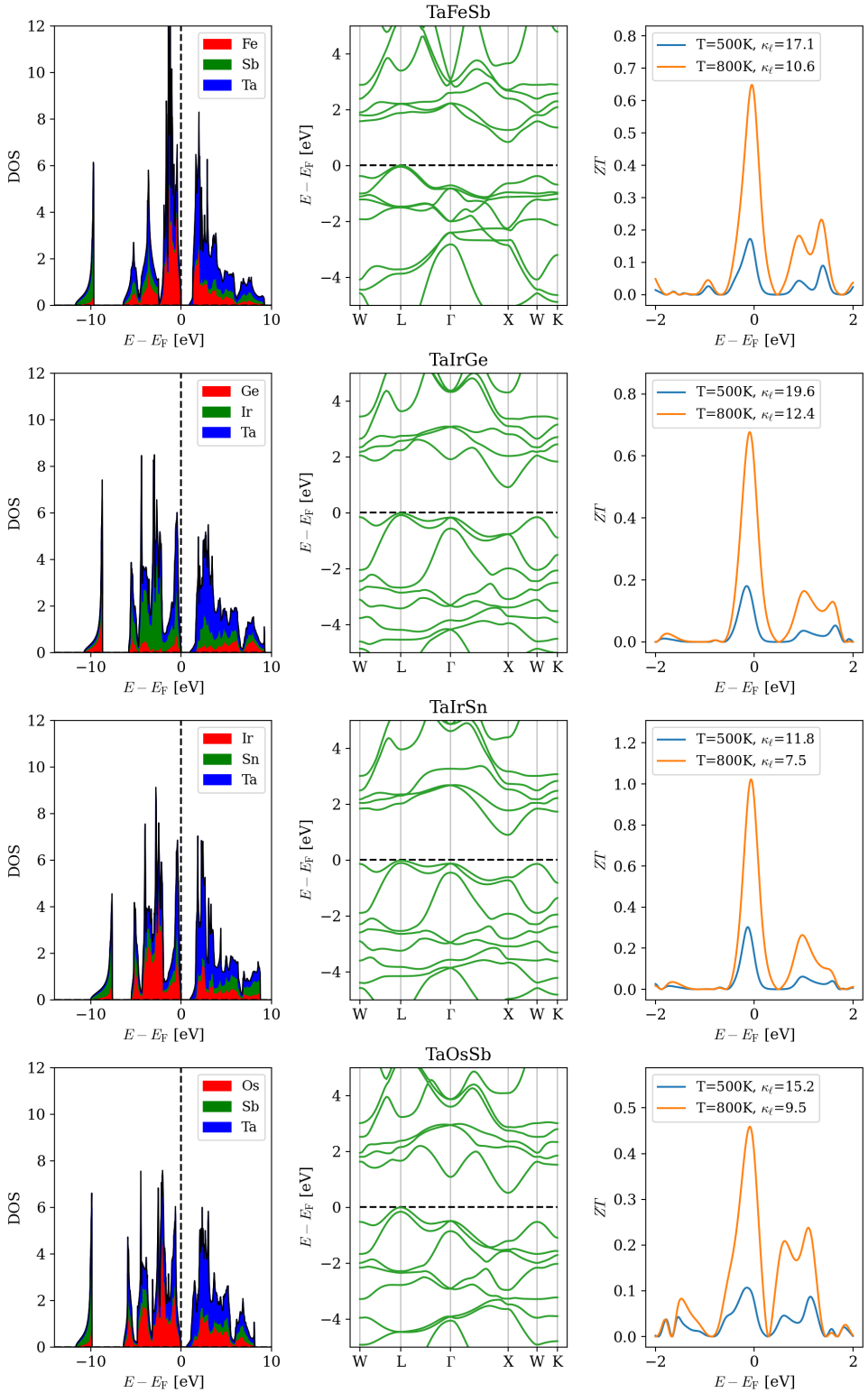

Figure A.7: LDOS, band structure and ZT for TaFeSb, TaIrGe, TaIrSn, and TaOsSb.

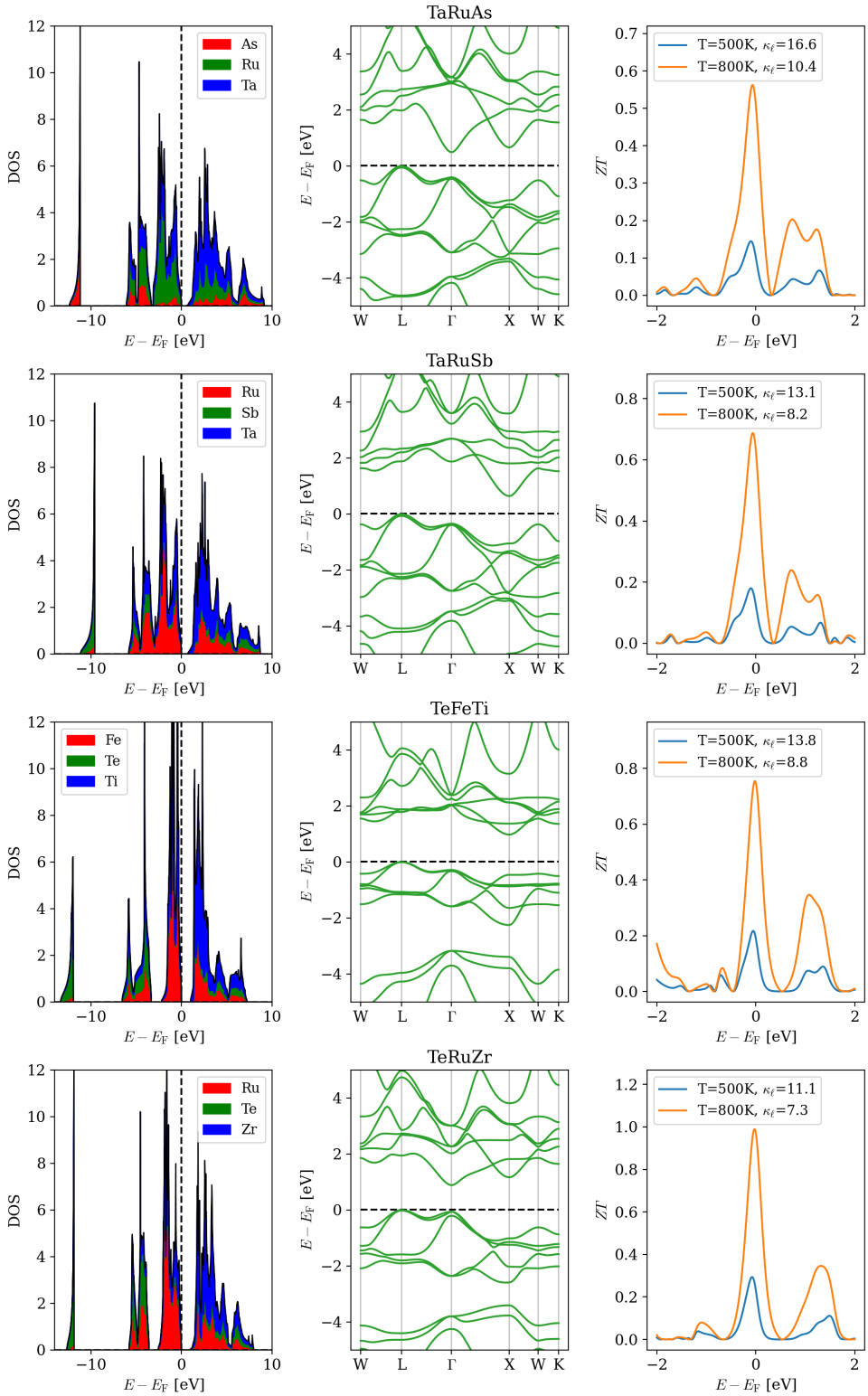

Figure A.8: LDOS, band structure and ZT for TaRuAs, TaRuSb, TeFeTi, and TeRuZr.

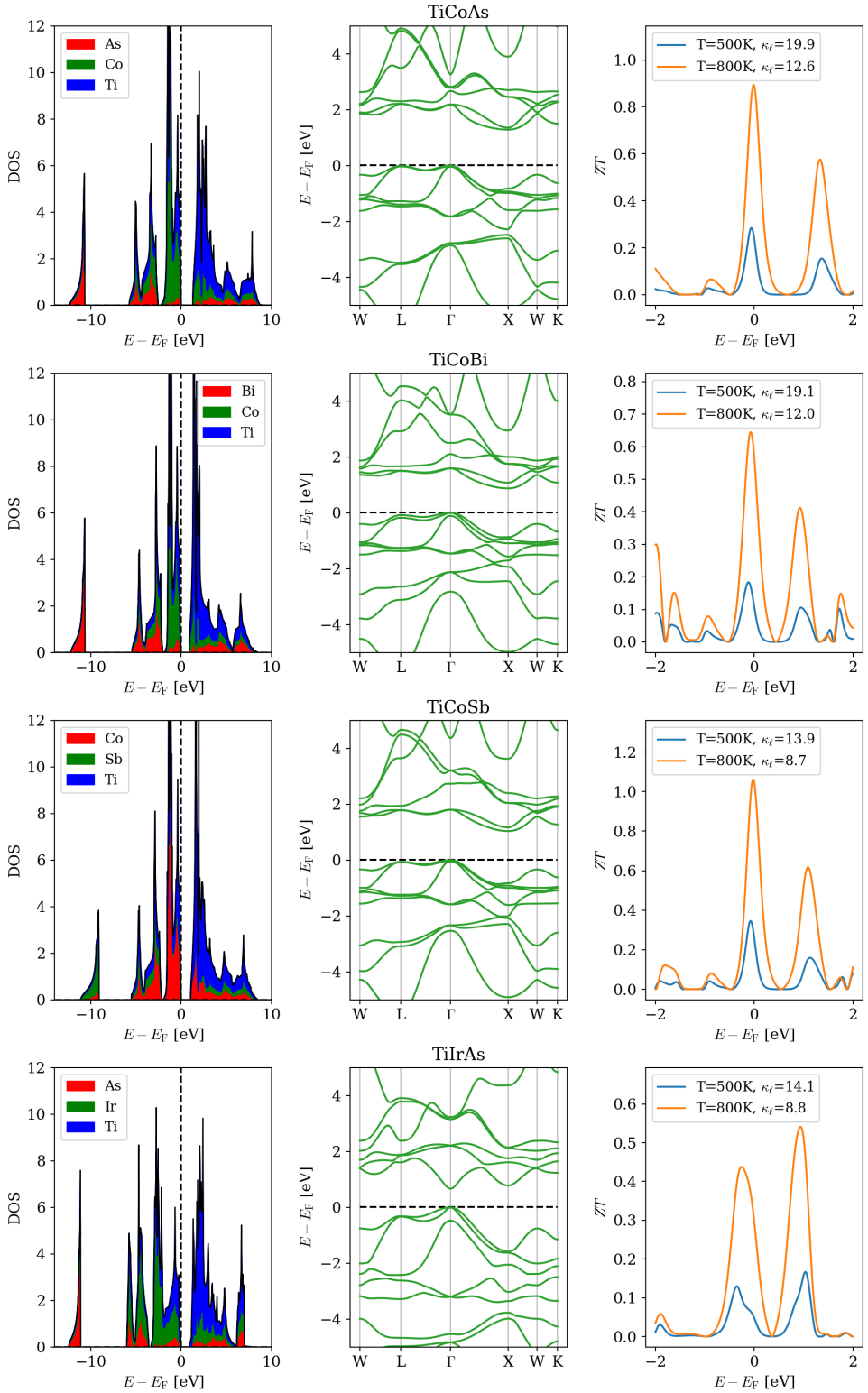

Figure A.9: LDOS, band structure and ZT for TiCoAs, TiCoBi, TiCoSb, and TiIrAs.

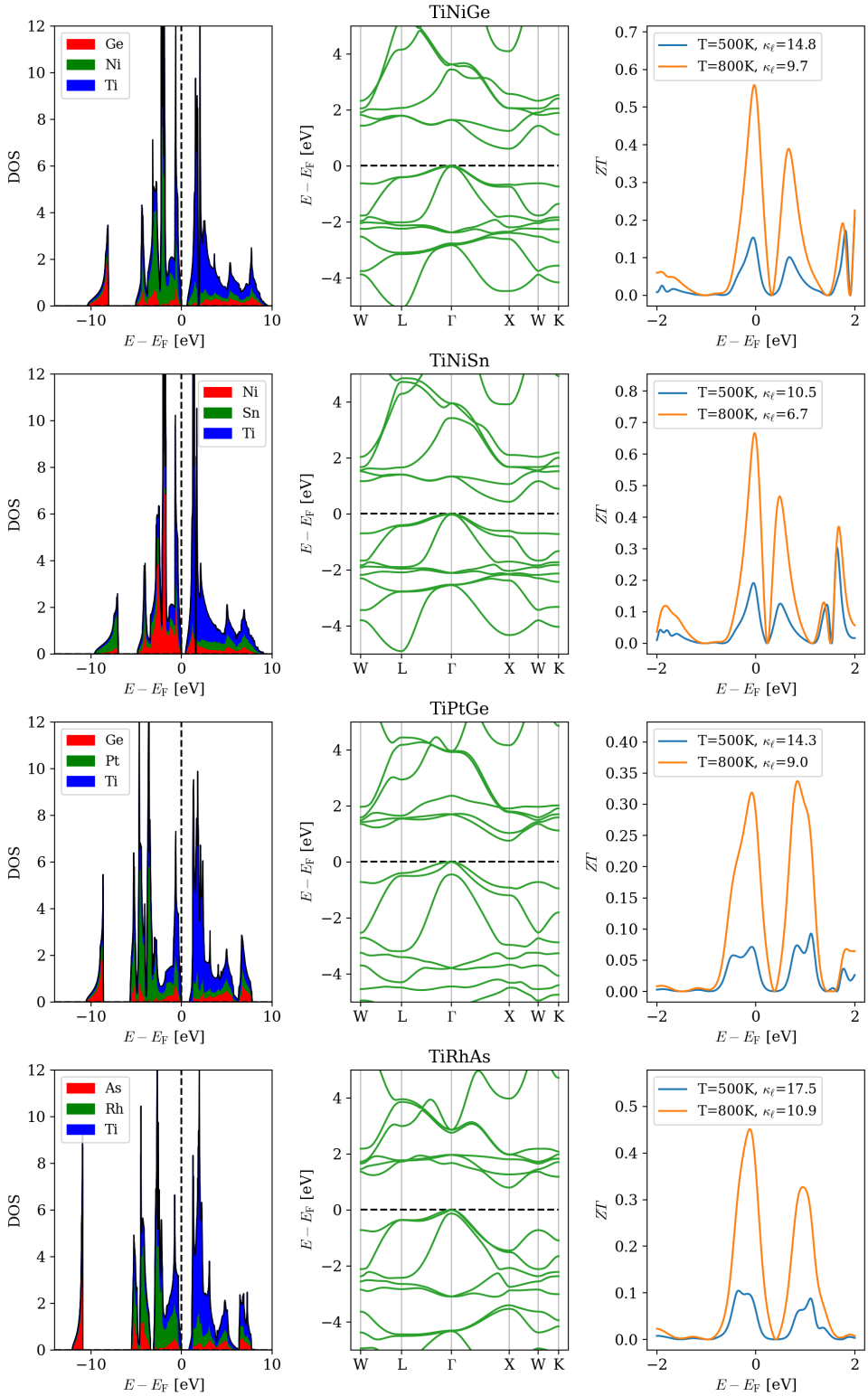

Figure A.10: LDOS, band structure and ZT for TiNiGe, TiNiSn, TiPtGe, and TiRhAs.

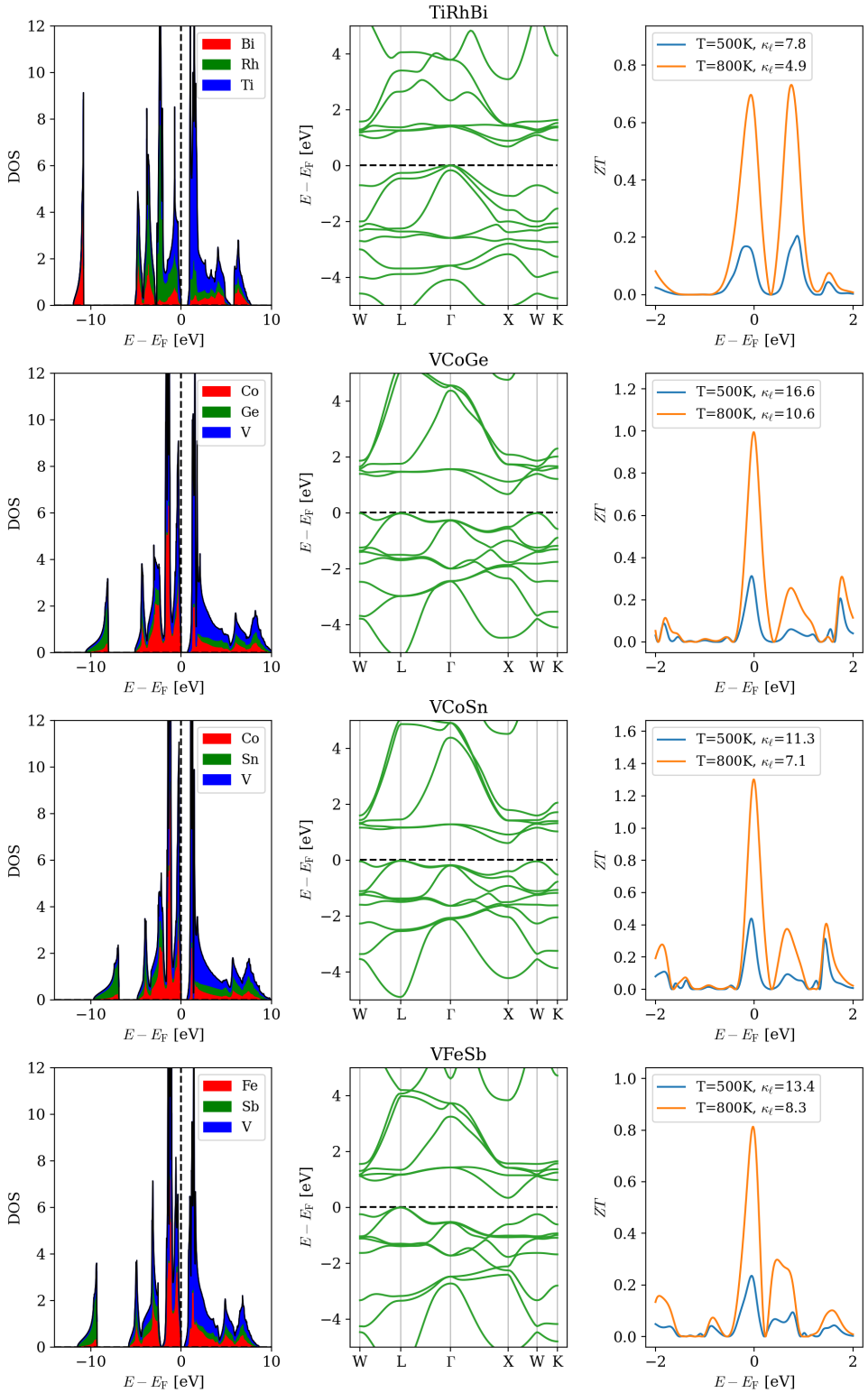

Figure A.11: LDOS, band structure and ZT for TiRhBi, VCoGe, VCoSn, and VFeSb.

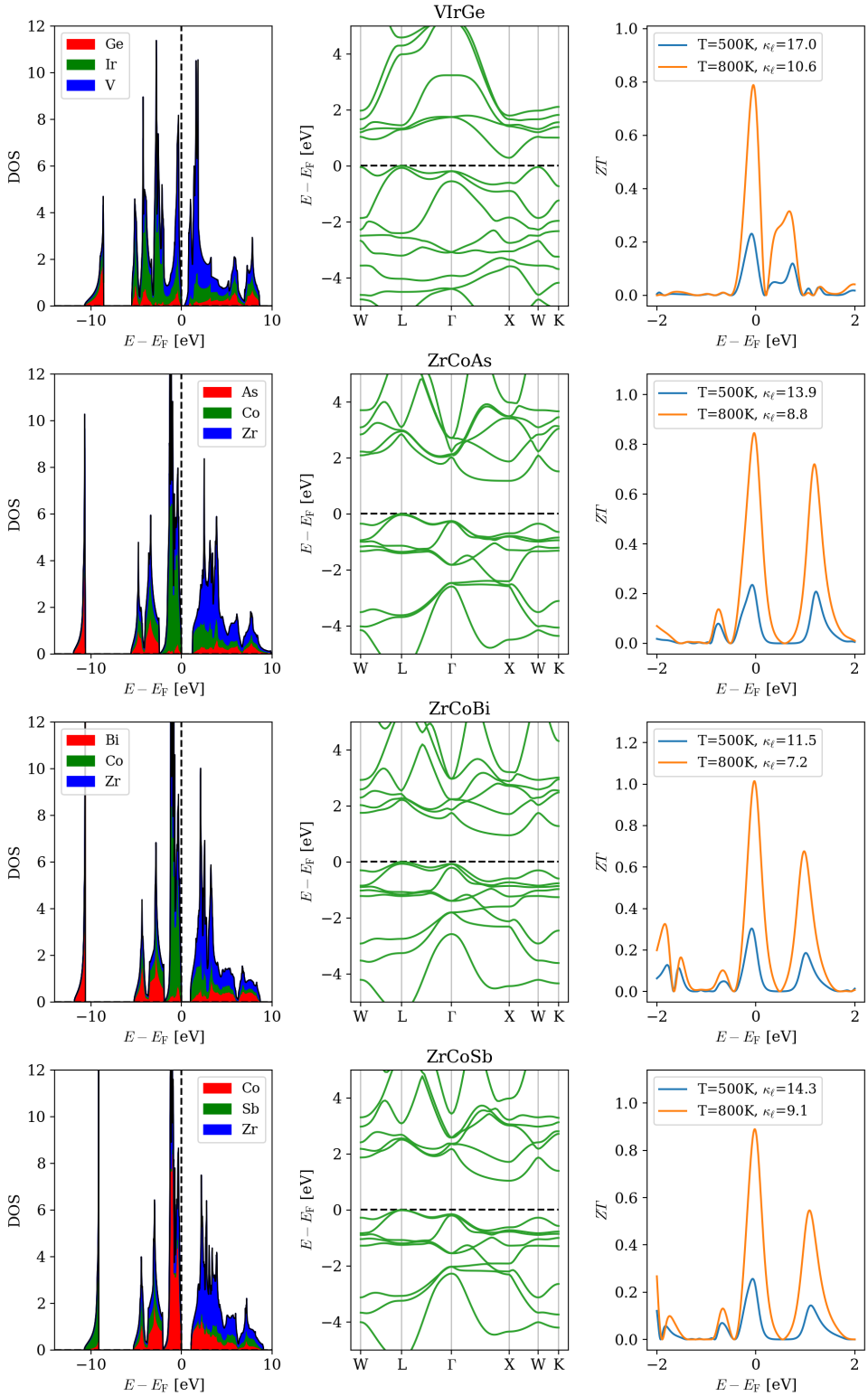

Figure A.12: LDOS, band structure and ZT for VIrGe, ZrCoAs, ZrCoBi, and ZrCoSb.

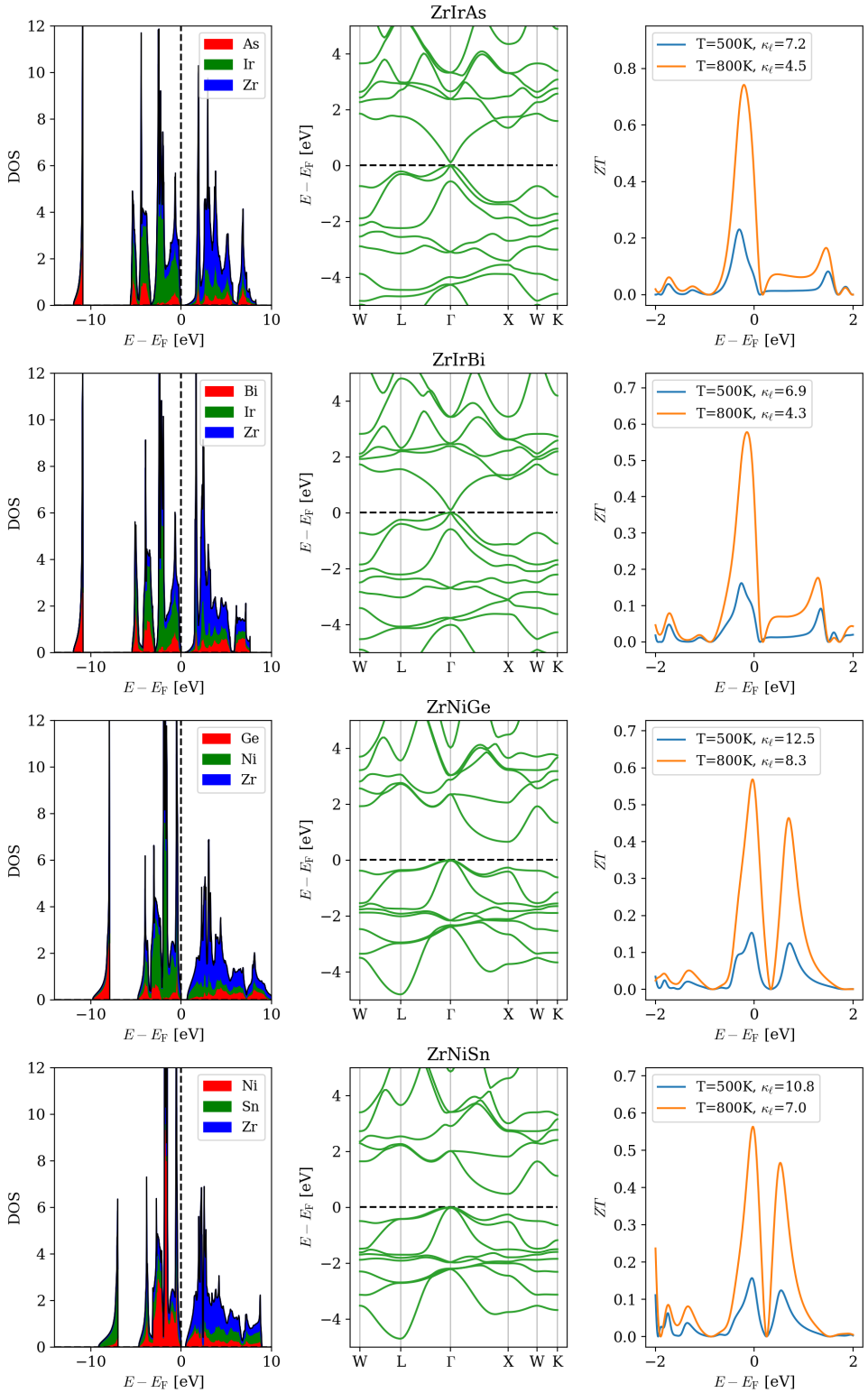

Figure A.13: LDOS, band structure and ZT for ZrIrAs, ZrIrBi, ZrNiGe, and ZrNiSn.

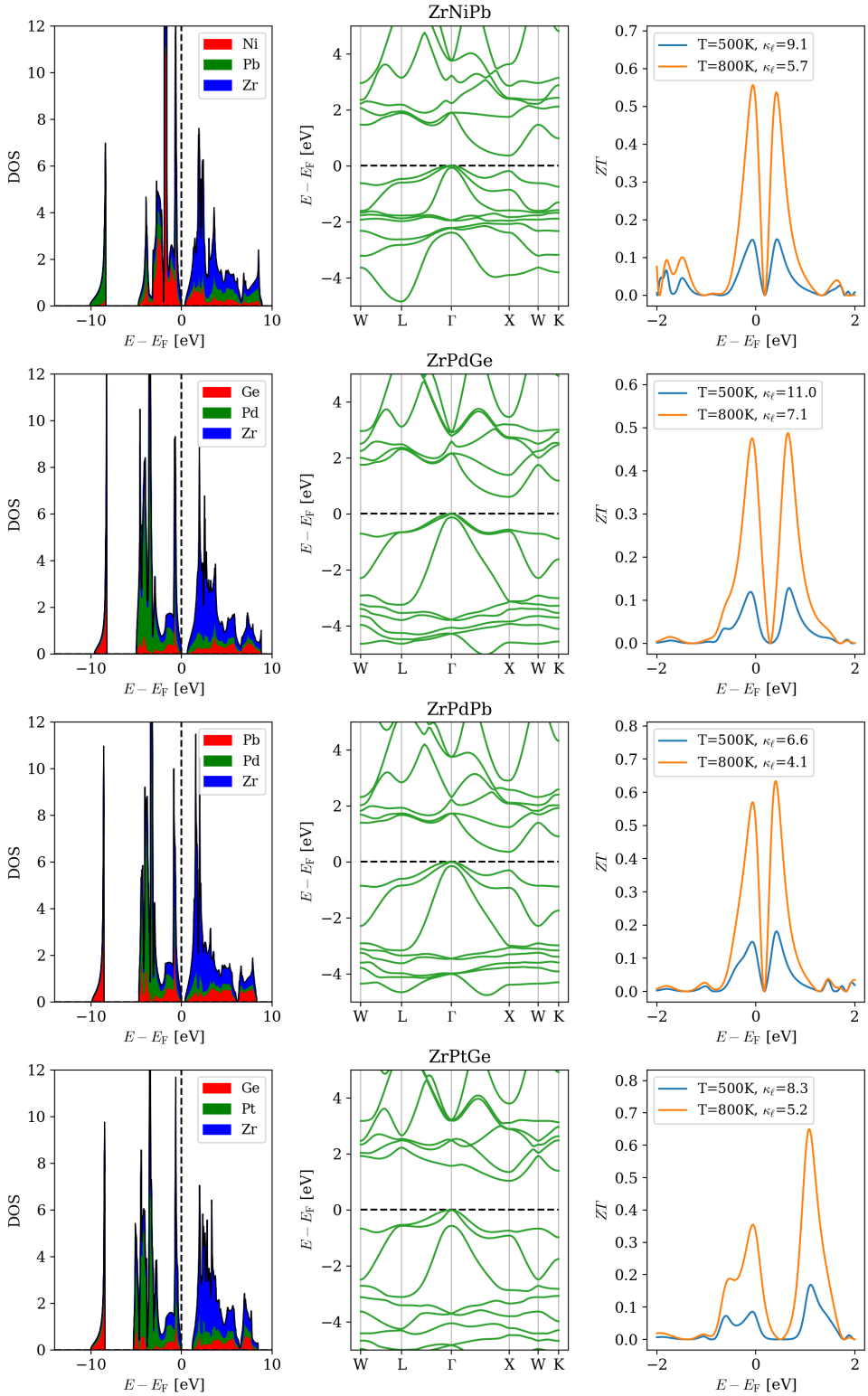

Figure A.14: LDOS, band structure and ZT for ZrNiPb, ZrPdGe, ZrPdPb, and ZrPtGe.

Appendix B

Volumetric band alignment

Figure B.1-B.7 show the power factor (PF), ZT, and band structure from VBA for the materials that are not shown in Results.

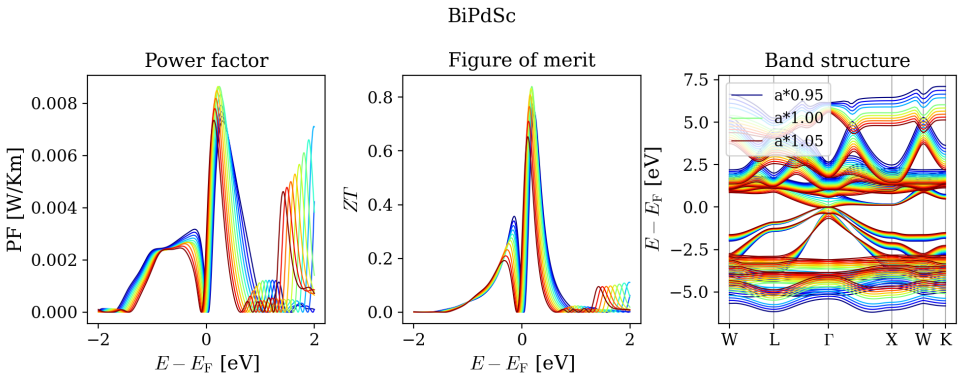

Figure B.1: PF, ZT, and band structure of BiPdSc at different volumes.

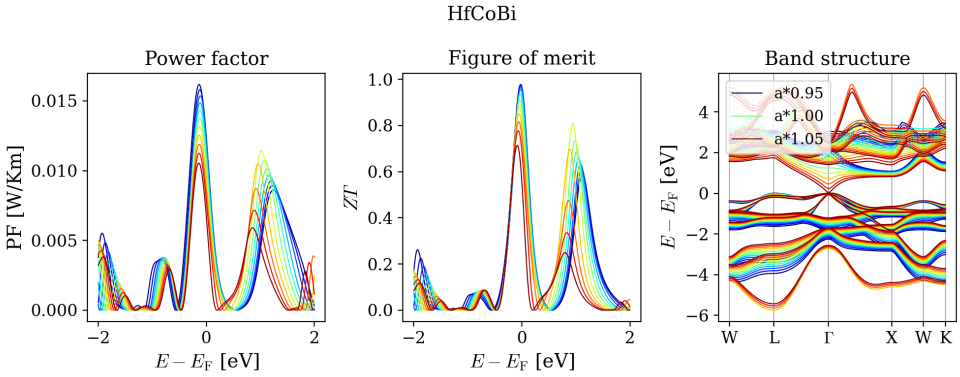

Figure B.2: PF, ZT, and band structure of HfCoBi at different volumes.

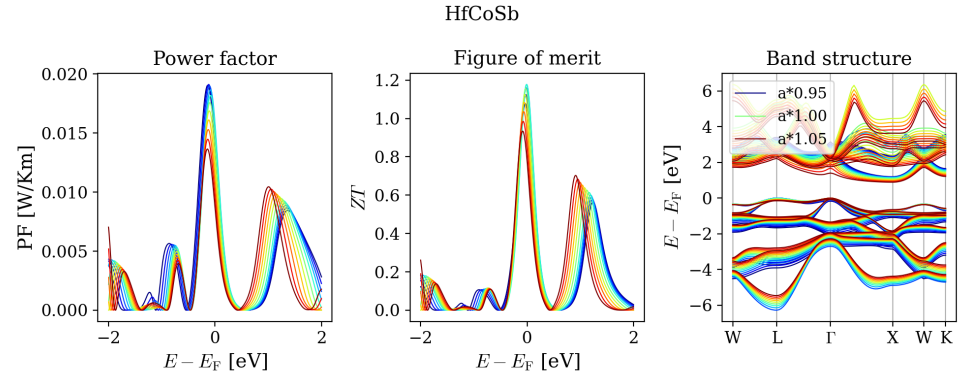

Figure B.3: PF, ZT, and band structure of HfCoSb at different volumes.

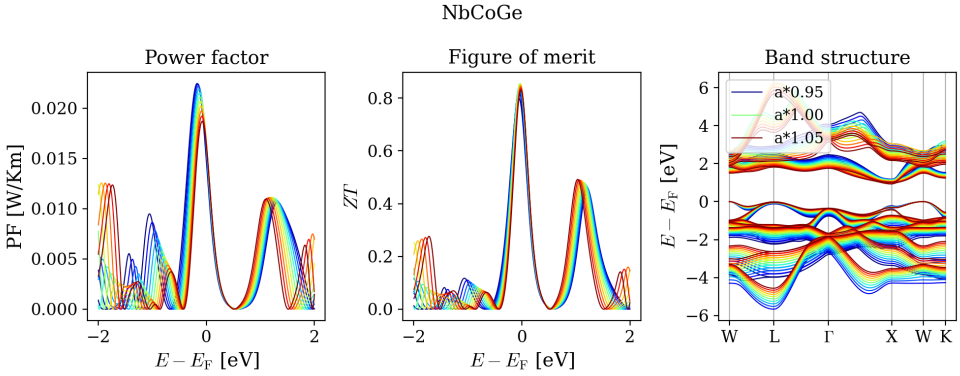

Figure B.4: PF, ZT, and band structure of NbCoGe at different volumes.

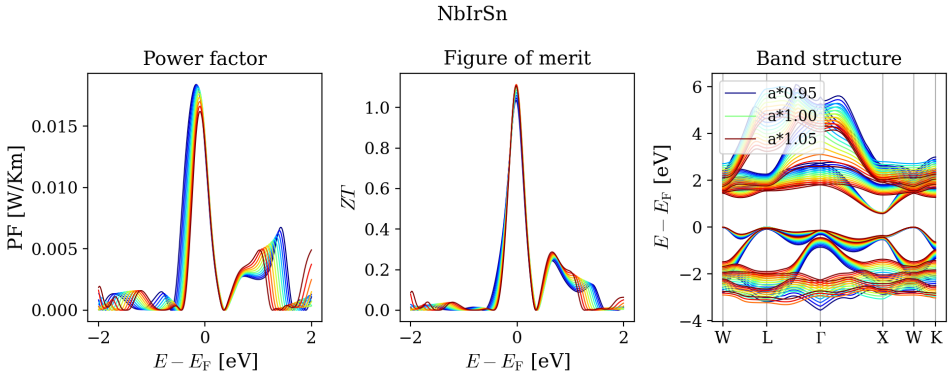

Figure B.5: PF, ZT, and band structure of NbIrSn at different volumes.

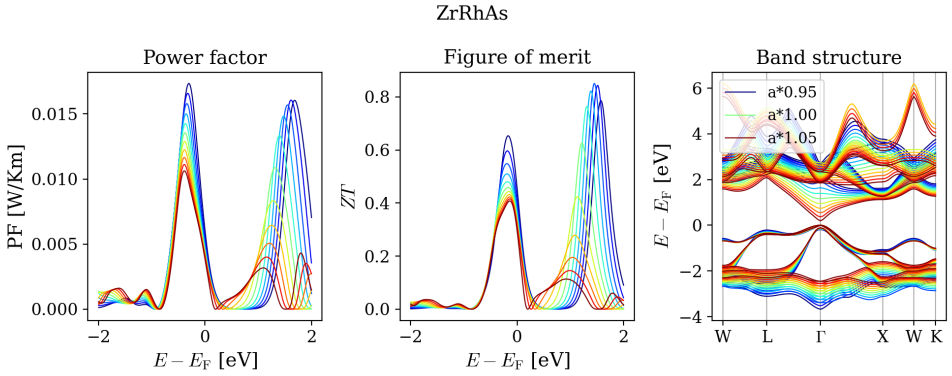

Figure B.6: PF, ZT, and band structure of ZrRhAs at different volumes.

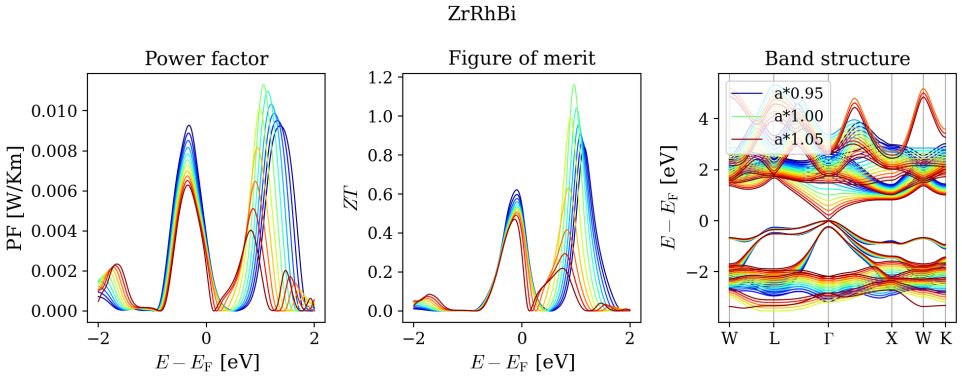

Figure B.7: PF, ZT, and band structure of ZrRhBi at different volumes.

Appendix C

Optimized TE properties of relaxed materials

In table C.1 and C.2 the electron transport properties, PF, and ZT at the doping level of maximum ZT for n-doping and p-doping at 800K. The relaxed lattice constants (a) and lattice thermal conductivities, provided by R. A. Tranås, are also listed.

Material	a [Å]	S [μV/K]	σ [10^4S/m]	κ_e [W/Km]	κ_ℓ [W/Km]	PF [mW/K^{2}m]	ZT
AlAuHf	6.27	-180	13.07	2.06	10.7	4.21	0.26
AlSiLi	5.94	-122	21.24	4.48	5.7	3.14	0.25
AsNiSc	5.84	-225	16.97	2.46	6.0	8.58	0.81
BaBiK	8.44	-161	2.61	0.51	1.24	0.67	0.31
BiNiSc	6.27	-170	24.74	4.6	4.35	7.18	0.64
BiPdSc	6.52	-180	24.98	4.32	3.39	8.09	0.84
CdPNa	6.43	-79	4.7	0.96	1.61	0.29	0.09
GeFeW	5.63	-120	15.67	3.08	10.71	2.26	0.13
HfCoAs	5.8	-236	20.18	2.62	7.24	11.26	0.91
HfCoBi	6.19	-223	18.82	2.66	7.54	9.34	0.73
HfCoSb	6.06	-215	17.78	2.68	7.8	8.19	0.63
HfIrSb	6.32	-100	90.27	16.42	8.63	9.06	0.29
HfNiGe	5.85	-206	14.52	2.21	7.18	6.17	0.53
HfNiSn	6.11	-188	15.31	2.57	7.12	5.4	0.45
HfPdSn	6.35	-193	13.01	2.15	5.91	4.83	0.48
HfRhBi	6.41	-88	59.14	11.8	4.37	4.61	0.23
LaPtSb	6.86	-192	22.79	4.16	0.53	8.4	1.43
LaRhTe	6.76	-313	4.47	0.59	0.7	4.38	2.72
LiZnSb	6.32	-207	11.14	2.13	2.36	4.77	0.85
NbCoGe	5.72	-196	26.24	4.05	12.68	10.04	0.48
NbCoSn	5.98	-213	19.04	2.77	7.69	8.65	0.66
NbFeAs	5.71	-164	10.97	1.79	13.86	2.93	0.15
NbFeSb	5.97	-172	10.17	1.65	9.36	2.99	0.22
NbIrGe	6.03	-168	9.82	1.62	10.89	2.78	0.18
NbIrSn	6.24	-179	8.98	1.47	7.29	2.88	0.26
NbOsSb	6.24	-143	13.93	2.84	7.44	2.85	0.22
NbRhSn	6.21	-187	8.76	1.38	6.23	3.05	0.32
NbRuAs	5.98	-149	13.38	2.53	12.87	2.97	0.15
NbRuSb	6.2	-161	11.07	2.02	7.9	2.87	0.23
TaCoGe	5.7	-192	18.0	3.02	9.69	6.63	0.42
TaCoSn	5.96	-194	15.13	2.44	8.36	5.69	0.42
TaFeAs	5.69	-180	8.32	1.26	9.34	2.69	0.2
TaFeSb	5.95	-179	8.55	1.34	10.62	2.73	0.18
TaIrGe	6.01	-166	10.54	1.71	12.4	2.9	0.16
TaIrSn	6.22	-181	8.91	1.4	7.47	2.93	0.26
TaOsSb	6.22	-170	10.3	1.81	9.53	2.96	0.21
TaRhSn	6.18	-187	7.75	1.21	7.13	2.7	0.26
TaRuAs	5.96	-144	16.4	3.05	10.39	3.41	0.2
TaRuSb	6.18	-177	9.29	1.51	8.21	2.91	0.24
TeFeTi	5.88	-179	15.83	2.93	8.81	5.09	0.35
TeRuZr	6.33	-124	48.37	9.87	7.26	7.41	0.35
TiCoAs	5.61	-208	27.29	3.8	12.57	11.78	0.58
TiCoBi	6.03	-195	19.81	2.61	11.98	7.52	0.41
TiCoSb	5.89	-207	21.21	3.04	8.7	9.06	0.62
TiIrAs	5.93	-162	41.34	7.15	8.81	10.8	0.54
TiNiGe	5.66	-196	15.17	2.27	9.66	5.8	0.39
TiNiSn	5.94	-195	13.5	2.1	6.68	5.11	0.47
TiPtGe	5.99	-182	14.72	2.59	9.0	4.88	0.34
TiRhAs	5.89	-158	25.63	4.71	10.91	6.38	0.33
TiRhBi	6.27	-207	15.83	2.52	4.89	6.77	0.73
VCoGe	5.51	-180	12.38	1.94	10.55	4.0	0.26
VCoSn	5.8	-191	11.3	1.68	7.15	4.13	0.37
VFeSb	5.79	-159	17.29	3.37	8.34	4.36	0.3
VIrGe	5.83	-108	87.62	15.16	10.6	10.15	0.32
ZrCoAs	5.86	-223	21.22	2.95	8.8	10.58	0.72
ZrCoBi	6.24	-218	17.37	2.51	7.24	8.24	0.68
ZrCoSb	6.11	-209	18.5	2.78	9.1	8.11	0.55
ZrIrAs	6.17	-90	6.42	1.26	4.52	0.52	0.07
ZrIrBi	6.49	-81	7.7	1.53	4.3	0.51	0.07
ZrNiGe	5.91	-202	14.96	2.25	8.26	6.1	0.46
ZrNiSn	6.16	-198	13.66	2.13	7.01	5.33	0.47
ZrNiPb	6.25	-198	13.62	2.22	5.73	5.33	0.54
ZrPdGe	6.18	-203	13.39	2.03	7.05	5.54	0.49
ZrPdPb	6.49	-204	11.5	1.88	4.14	4.77	0.63
ZrPtGe	6.22	-217	12.48	2.03	5.23	5.89	0.65
ZrRhAs	6.12	-214	21.04	3.07	9.2	9.6	0.63
ZrRhBi	6.45	-243	16.22	2.04	4.59	9.61	1.16

Table C.1: Electron transport properties at maximum ZT for n-doped materials at 800K, together with lattice constant and lattice thermal conductivity.

Material	a [Å]	S [μV/K]	σ [10^4S/m]	κ_e [W/K^{2}m]	κ_ℓ [W/Km]	PF [mW/K^{2}m]	ZT
AlAuHf	6.27	186	17.52	2.86	10.7	6.06	0.36
AlSiLi	5.94	157	24.1	4.58	5.7	5.91	0.46
AsNiSc	5.84	190	12.42	2.03	6.0	4.5	0.45
BaBiK	8.44	205	4.33	0.36	1.24	1.82	0.91
BiNiSc	6.27	124	20.41	4.2	4.35	3.14	0.29
BiPdSc	6.52	117	18.38	3.87	3.39	2.51	0.28
CdPNa	6.43	228	10.53	1.89	1.61	5.49	1.26
GeFeW	5.63	214	36.39	5.74	10.71	16.63	0.81
HfCoAs	5.8	244	27.25	3.3	7.24	16.19	1.23
HfCoBi	6.19	228	23.16	2.99	7.54	12.0	0.91
HfCoSb	6.06	238	27.72	3.03	7.8	15.65	1.16
HfIrSb	6.32	159	17.45	3.48	8.63	4.44	0.29
HfNiGe	5.85	205	15.07	2.28	7.18	6.31	0.53
HfNiSn	6.11	192	16.05	2.6	7.12	5.91	0.49
HfPdSn	6.35	204	13.67	2.12	5.91	5.69	0.57
HfRhBi	6.41	195	11.26	2.03	4.37	4.26	0.53
LaPtSb	6.86	161	5.26	1.18	0.53	1.36	0.64
LaRhTe	6.76	297	3.31	0.69	0.7	2.92	1.68
LiZnSb	6.32	172	11.0	2.22	2.36	3.26	0.57
NbCoGe	5.72	223	37.64	4.86	12.68	18.76	0.86
NbCoSn	5.98	242	29.29	3.29	7.69	17.13	1.25
NbFeAs	5.71	208	29.23	4.36	13.86	12.62	0.55
NbFeSb	5.97	223	24.18	3.5	9.36	11.99	0.75
NbIrGe	6.03	224	30.72	4.31	10.89	15.4	0.81
NbIrSn	6.24	241	25.3	3.4	7.29	14.64	1.1
NbOsSb	6.24	200	22.06	3.73	7.44	8.84	0.63
NbRhSn	6.21	238	24.81	3.63	6.23	14.04	1.14
NbRuAs	5.98	201	25.52	3.99	12.87	10.32	0.49
NbRuSb	6.2	219	21.46	3.42	7.9	10.28	0.73
TaCoGe	5.7	233	32.6	4.07	9.69	17.66	1.03
TaCoSn	5.96	234	30.85	3.47	8.36	16.89	1.14
TaFeAs	5.69	220	23.74	3.59	9.34	11.44	0.71
TaFeSb	5.95	213	25.87	3.8	10.62	11.7	0.65
TaIrGe	6.01	208	34.52	5.26	12.4	14.94	0.68
TaIrSn	6.22	231	27.04	3.78	7.47	14.38	1.02
TaOsSb	6.22	191	20.62	3.58	9.53	7.52	0.46
TaRhSn	6.18	245	30.86	3.32	7.13	18.54	1.42
TaRuAs	5.96	209	22.57	3.59	10.39	9.83	0.56
TaRuSb	6.18	218	21.12	3.43	8.21	10.0	0.69
TeFeTi	5.88	220	22.92	2.99	8.81	11.14	0.75
TeRuZr	6.33	236	23.57	3.36	7.26	13.13	0.99
TiCoAs	5.61	227	36.23	4.11	12.57	18.64	0.89
TiCoBi	6.03	209	29.09	3.77	11.98	12.69	0.64
TiCoSb	5.89	234	28.96	3.24	8.7	15.84	1.06
TiIrAs	5.93	143	49.97	9.75	8.81	10.16	0.44
TiNiGe	5.66	210	20.02	2.96	9.66	8.81	0.56
TiNiSn	5.94	213	17.05	2.57	6.68	7.71	0.67
TiPtGe	5.99	183	13.49	2.33	9.0	4.51	0.32
TiRhAs	5.89	183	26.7	4.99	10.91	8.97	0.45
TiRhBi	6.27	211	14.67	2.6	4.89	6.53	0.7
VCoGe	5.51	232	33.4	3.86	10.55	17.93	0.99
VCoSn	5.8	241	27.78	2.81	7.15	16.2	1.3
VFeSb	5.79	217	26.28	3.86	8.34	12.4	0.81
VIrGe	5.83	212	33.29	4.65	10.6	15.02	0.79
ZrCoAs	5.86	226	25.98	3.7	8.8	13.21	0.85
ZrCoBi	6.24	229	25.03	3.11	7.24	13.13	1.01
ZrCoSb	6.11	225	27.76	3.53	9.1	14.05	0.89
ZrIrAs	6.17	180	30.22	6.0	4.52	9.76	0.74
ZrIrBi	6.49	177	18.27	3.6	4.3	5.7	0.58
ZrNiGe	5.91	210	17.74	2.78	8.26	7.85	0.57
ZrNiSn	6.16	209	14.93	2.25	7.01	6.53	0.56
ZrNiPb	6.25	195	14.92	2.45	5.73	5.69	0.56
ZrPdGe	6.18	197	14.31	2.31	7.05	5.56	0.48
ZrPdPb	6.49	197	11.41	2.05	4.14	4.41	0.57
ZrPtGe	6.22	192	7.86	1.28	5.23	2.89	0.35
ZrRhAs	6.12	172	29.08	5.81	9.2	8.61	0.46
ZrRhBi	6.45	198	11.57	2.2	4.59	4.53	0.53

Table C.2: Electron transport properties at maximum ZT for p-doped materials at 800K, together with lattice constant and lattice thermal conductivity.

Appendix D

Lattice thermal conductivity

Table D.1 lists the values of lattice thermal conductivity used for comparing ZT values with *Thermoelectric transport trends in group 4 half-Heusler alloys*[13] in Figure 5.1 are listed. In that article, various phonon scattering mechanisms were included when calculating κ_ℓ. These values were provided in the Supplementary Material of the article.

Material	κ_ℓ [W/Km]
HfCoAs	1.73
HfCoBi	2.0
HfCoSb	2.08
HfIrSb	3.08
HfNiGe	1.59
HfNiSn	1.83
HfPdSn	2.03
HfRhBi	1.7
TiCoAs	1.7
TiCoBi	1.12
TiCoSb	2.02
TiIrAs	2.45
TiNiGe	1.57
TiNiSn	1.77
TiPtGe	2.14
TiRhAs	1.57
TiRhBi	0.78
ZrCoAs	1.6
ZrCoBi	1.6
ZrCoSb	2.58
ZrIrAs	2.34
ZrIrBi	1.69
ZrNiGe	1.64
ZrNiPb	1.32
ZrNiSn	2.22
ZrPdGe	1.72
ZrPdPb	1.21
ZrPtGe	2.21
ZrRhAs	1.85
ZrRhBi	1.26

Table D.1: Lattice thermal conductivity used for calculation of ZT in Figure 5.1. Provided by *Thermoelectric transport trends in group 4 half-Heusler alloys*[13].

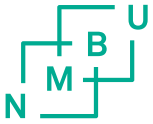

Norges miljø- og biovitenskapelige universitet
Noregs miljø- og biovitskapelege universitet
Norwegian University of Life Sciences

Postboks 5003
NO-1432 Ås
Norway